Fachbereich 13 Physik
Institut für Theoretische Physik,
Goethe Universität Frankfurt am Main

Master Thesis

Structure of hybrid static potential flux tubes from SU(2) and SU(3) lattice Yang-Mills-theory

Lasse Müller

Frankfurt am Main
24. Juli 2019

Advisor and first supervisor:
Prof. Dr. Marc Wagner
Institut für Theoretische Physik
Goethe Universität Frankfurt am Main

Second supervisor:
Prof. Dr. Owe Philipsen
Institut für Theoretische Physik
Goethe Universität Frankfurt am Main

Selbstständigkeitserklärung

Hiermit erkläre ich, dass ich die Arbeit selbstständig und ohne Benutzung anderer als der angegebenen Quellen und Hilfsmittel verfasst habe. Alle Stellen der Arbeit, die wörtlich oder sinngemäß aus Veröffentlichungen oder aus anderen fremden Texten entnommen wurden, sind von mir als solche kenntlich gemacht worden. Ferner erkläre ich, dass die Arbeit nicht - auch nicht auszugsweise - für eine andere Prüfung verwendet wurde.

Ort, Datum: _____

Unterschrift: _____ (Lasse Müller)

Abstract

In this work we compute chromoelectric and chromomagnetic flux densities for hybrid static potentials in SU(2) and SU(3) lattice Yang-Mills theory. We show results for quantum numbers $\Lambda_\eta^\epsilon = \Sigma_g^+, \Sigma_g^-, \Sigma_u^+, \Sigma_u^-, \Pi_g, \Pi_u, \Delta_g, \Delta_u$, where the flux densities of five of them were studied for the first time. The flux tube structure changes significantly for hybrid static potentials compared to the ordinary static potential. We find strong localized peaks which can be interpreted as valence gluons. Furthermore, our results are consistent with investigations using pNRQCD.

Content

1. Introduction

According to the standard model of particle physics all matter is composed of spin-$\frac{1}{2}$ particles, so called fermions. The four fundamental forces, gravity, electromagnetism, weak force and strong force, are mediated between those particles via so called gauge bosons, particles with integer spin.
The strong interaction between quarks and gluons is exerted by so called color charges. Several experiments showed that there are three different charges labeled with the colors red, green and blue. In contrast to the photons in quantum electrodynamics, gluons also carry color charge. Consequently, the quantum field theory of the strong interaction, quantum chromodynamics (QCD), is described by a non-abelian gauge symmetry group SU(3).

The coupling constant of the strong force becomes large at low energies and large distances, making it impossible to work with perturbation theory in this regime. Hence, a valid approach is to introduce a lattice representing a discretized spacetime and perform numerical simulations of the physical system.

The elementary fermions carrying color charge are referred to as quarks, which come in 6 flavours: up, down, strange, charm, bottom and top. In the standard quark model quarks can form either mesonic quark-antiquark ($q\bar{q}$) states or baryonic (anti)quark-(anti)quark-(anti)quark (qqq or $\bar{q}\bar{q}\bar{q}$) states with corresponding quantum numbers (angular momentum, parity, charge etc.) dependent on the (anti-)flavour of the quarks. This is due to the property of confinement: quarks can never appear as single particles, but always as color singlets, i.e. color neutral objects. There are, anyhow, experimental observations of quark states which can not be explained by this simple quark model [1]. These are for example the $J^{PC} = 1^{-+}$ states $\pi_1(1400)$ and $\pi_2(1600)$.

One explanation of these exotic mesons would be the existence of tetraquarks, bound states of two quarks and two antiquarks ($qq\bar{q}\bar{q}$), which again form a color singlet and, thus, are technically possible. Another explanation would be excited gluon structures in a quark-antiquark state, contributing to the quantum numbers (hybrid mesons). The latter is the system investigated in this work.
Hybrid mesons are also a topic of large interest for experimentalist as the PANDA experiment at FAIR is planning to search for exotic matter in the form of hybrid mesons and glueballs.
We study the limit of infinitely heavy i.e. static quarks. In the past hybrid static potentials were mainly investigated in order to obtain masses of heavy hybrid mesons using the Born-Oppenheimer approximation [2–26]. In this work on the other hand we consider the flux tubes of such meson states. While the flux tubes of the ordinary static potential are subject of studies for a long time [27–42]) we are among the first to study hybrid static potential flux tubes [43–46].

The aim of this work is to get an insight on the effects of excitations in the gluon sector on the structure of flux tubes from lattice simulations using pure gauge theory. We compute the square of chromoelectric and chromomagnetic field strength components for the ordinary static potential $\Lambda_\eta^\epsilon = \Sigma_\eta^\epsilon$ and the seven lowest energy hybrid static potentials with quantum numbers $\Lambda_\eta^\epsilon = \Sigma_g^-, \Sigma_u^+, \Sigma_u^-, \Pi_g, \Pi_u, \Delta_g, \Delta_u$.

This work is structured as follows. In section 2 we briefly introduce SU(2) and SU(3) lattice Yang-Mills theory and fix some notations. In the following section 3 we derive how to compute the static potential and the square of field strength components on the lattice. Section 4 addresses the formulation of quantum numbers for hybrid static potentials Λ_η^ϵ and how to construct operators generating corresponding trial states on the lattice. Section 5 starts with a detailed description of the lattice setup followed by the discussion of systematic errors before showing numerical results on the flux densities of hybrid static potentials. Finally we give a short summary and outlook in section 6.

2. SU(2) and SU(3) lattice Yang-Mills theory

In this work we will perform simulations in both SU(2) and SU(3) lattice Yang-Mills theory For the investigation of a meson system with static quarks it is a valid approach to reduce the number of different colors down to two by considering the gauge group SU(2) instead. This gives similar results and yields less expensive simulations making it a feasible choice for qualitative investigations.
In pure lattice Yang-Mills theory there are only gauge fields to consider while fermions, which are a major challenge to simulate on the lattice, are absent.
In order to make the kinetic term of fermions in the QCD action invariant under gauge transformations one needs to introduce a covariant derivative. It can be expressed by the parallel transporter

$$U(x,y) = P\left(\exp\left[ig\int_x^y \mathrm{d}z_\mu \mathcal{A}^\mu(z)\right]\right) \in SU(N) \tag{2.1}$$

where g is the coupling constant, $\mathcal{A}_\mu = A^a_\mu T^a$ the gauge field with the generators of the SU(N) algebra T^a and P denotes path ordering. In the case of SU(2) these correspond to the Pauli-matrices and for SU(3) to the Gell-Mann-matrices.
On the lattice the parallel transport (2.1) from one lattice site ($x \in \mathbb{N}^4$) to a neighboring one in direction μ will be referred to as link variable

$$U_\mu(x) = \exp\left(iga\mathcal{A}_\mu\right), \tag{2.2}$$

with lattice spacing a.
We can obtain gauge invariant observables by constructing closed paths of link variables on the lattice. We denote a straight path of link variables starting at x and ending at $x + r\hat{e}_\mu$ in direction μ as

$$S_\mu(x,r) = P\left(\prod_{k=0}^{r-1} U_\mu(x + ak\hat{e}_\mu)\right) \tag{2.3}$$

An important lattice observable for studying the static quark-antiquark potential is the Wilson loop

$$W_{\mu\nu}(x,r,t) = \mathrm{Tr}\left[S_\mu(x,r)\cdot S_\nu(x+\hat{e}_\mu r,t)\cdot S^\dagger_\mu(x+\hat{e}_\nu t,r)\cdot S^\dagger_\nu(x,t)\right], \tag{2.4}$$

where the simplest non-trivial Wilson loop is called plaquette

$$P_{\mu\nu}(x) = \mathrm{Tr}\left[U_\mu(r)\cdot U_\nu(r+a\mu)\cdot U^\dagger_\mu(r+a\nu)\cdot U^\dagger_\nu(r)\right] \tag{2.5}$$

In this work the Wilson loop will only appear in the z-0-plane and is independent of x when performing the path integral expectation value $\langle ... \rangle$. Consequently, we set

$$\langle W(r,t_2,t_0)\rangle \equiv \langle W_{z0}(x,r,t_2-t_0)\rangle\,. \tag{2.6}$$

3. Static $Q\bar{Q}$ - potentials in SU(2) and SU(3) lattice Yang-Mills theory

3.1. Static $Q\bar{Q}$ potential

We construct a two point correlation function for a trial state of a quark at $(\mathbf{x}, t_0)$ and an antiquark at $(\mathbf{y}, t_0)$ propagating to t_2 (we already label the times t_0 and t_2 in order to keep the notation consistent throughout this work as we will introduce an intermediate time t_1 in the next chapter)

$$\begin{aligned}\mathcal{C}_{Q\bar{Q}}(\mathbf{x},\mathbf{y},t_2,t_0) &= \langle\Omega|\mathcal{O}^\dagger(\mathbf{x},t_2;\mathbf{y},t_2)\mathcal{O}(\mathbf{x},t_0;\mathbf{y},t_0)|\Omega\rangle \\ &= \langle\Omega|\bar{Q}(\mathbf{y},t_2)U(\mathbf{y},t_2;\mathbf{x},t_2)Q(\mathbf{x},t_2)\bar{Q}(\mathbf{x},t_0)U(\mathbf{x},t_0;\mathbf{y},t_0)Q(\mathbf{y},t_0)|\Omega\rangle\,.\end{aligned} \tag{3.1}$$

Here $|\Omega\rangle$ denotes the vacuum, $\bar{Q}(\mathbf{x},t)$ and $Q(\mathbf{y},t)$ are operators creating a spinless quark-antiquark pair and we omit all color indices in favor of readability. After a lengthy calculation which can be found in [47] it is shown, that this two point correlation function is proportional to the path integral expectation value of the Wilson loop (2.4) in temporal and $\mathbf{y}-\mathbf{x} \equiv (0,0,z)$ direction

$$\mathcal{C}_{Q\bar{Q}}(\mathbf{x},\mathbf{y},t_2,t_0) \propto \langle W(r,t_2,t_0)\rangle\,. \tag{3.2}$$

Starting at the first line of eq. (3.1) we can also perform a time evolution of the operators and insert a complete basis of energy eigenstates $|n\rangle$ to obtain

$$\begin{aligned}\mathcal{C}_{Q\bar{Q}}(t_2,t_0) = \langle\Omega|\mathcal{O}^\dagger(t_2)\mathcal{O}(t_0)|\Omega\rangle &= \langle\Omega|e^{H(t_2-t_0)}\mathcal{O}^\dagger(t_0)e^{-H(t_2-t_0)}\mathcal{O}(t_0)|\Omega\rangle \\ &= \sum_n \langle\Omega|e^{H(t_2-t_0)}\mathcal{O}^\dagger(t_0)|n\rangle\,\langle n|e^{-H(t_2-t_0)}\mathcal{O}(t_0)|\Omega\rangle \\ &= \sum_n |\langle\Omega|\mathcal{O}(t_0)|n\rangle\,|^2 e^{-(E_n-E_\Omega)(t_2-t_0)}.\end{aligned} \tag{3.3}$$

In the limit of large (t_2-t_0) only the ground state will contribute since all other states are exponentially suppressed. This leads to

$$\lim_{t_2-t_0\to\infty} \mathcal{C}_{Q\bar{Q}}(t_2,t_0) = F(t_0)e^{-(E_0-E_\Omega)(t_2-t_0)} = F(t_0)e^{-V_{Q\bar{Q}}(t_2-t_0)}, \tag{3.4}$$

where $V_{Q\bar{Q}}$ is the static $Q\bar{Q}$ potential and

$$F(t_0) = |\langle\Omega|\mathcal{O}(t_0)|0\rangle\,|^2 \tag{3.5}$$

denotes the overlap of the initial trial state with the ground state of the system. Comparing eq. (3.2) and eq. (3.4) we can extract the static potential between quark and antiquark in the continuum as

$$V_{Q\bar{Q}}(r) = \lim_{a\to 0}\lim_{t_2-t_0\to\infty} V_{\text{eff}}(r) = \lim_{a\to 0}\lim_{t_2-t_0\to\infty} \frac{1}{a}\ln\left[\frac{\langle W(r,t_2-t_0)\rangle}{\langle W(r,t_2-t_0+a)\rangle}\right], \tag{3.6}$$

where we used the definition of the effective potential as the temporal forward derivative.

3.2. Squared field strengths components

On the lattice we can find a correspondence of the plaquette $P_{\mu\nu}$ to the field strength tensor in the continuum. Plugging in eq. (2.2) into eq. (2.5) we obtain

$$P_{\mu\nu} = \mathrm{Tr}\left[e^{iga^2\mathcal{F}_{\mu\nu}}\right] \tag{3.7}$$

with $\mathcal{F}_{\mu\nu} = F^a_{\mu\nu}T^a$. Performing a second order Taylor expansion yields

$$\begin{aligned} P_{\mu\nu} &= \mathrm{Tr}\left[1 + iga^2\mathcal{F}_{\mu\nu} - \frac{g^2a^4}{2}\mathcal{F}^2_{\mu\nu} + \mathcal{O}(a^6)\right] \\ &= N + iga^2F^a_{\mu\nu}\mathrm{Tr}\left(T^a\right) - \frac{g^2a^4}{2}F^a_{\mu\nu}F^b_{\mu\nu}\mathrm{Tr}\left(T^aT^b\right) + \mathcal{O}(a^6) \\ &= N - \frac{g^2a^4}{4}\left(F^a_{\mu\nu}F^a_{\mu\nu}\right) \\ \Leftrightarrow F^a_{\mu\nu}F^a_{\mu\nu} + \mathcal{O}(a^2) &= \frac{4}{g^2a^4}\left(N - P_{\mu\nu}\right), \end{aligned} \tag{3.8}$$

where we used in the second step that the generators of any SU(N) Lie algebra are traceless and $\mathrm{Tr}(T^aT^b) = \delta^{ab}/2$. Since there is no sum over μ and ν we can always identify $F^a_{\mu\nu}F^a_{\mu\nu}$ with $E^a_jE^a_j$ or $B^a_jB^a_j$ (no sum over j). So, while the field strength components themselves are obviously not a gauge invariant quantity, the square of them actually is and as such can be measured on the lattice without gauge fixing. In the following F^a_j denotes either E^a_j or B^a_j. Additionally, we introduce $F^2_j(x) = \sum_a F^a_j(x)F^a_j(x)$ (again, with no sum over j).

We want to compute the change of the field strength components when generating a quark-antiquark pair in the vacuum. Consequently we also need to subtract the vacuum contribution

$$\Delta F^2_j \equiv \langle F^2_j\rangle_{Q\bar{Q}} - \langle F^2_j\rangle_{\Omega}\,. \tag{3.9}$$

This expectation value represents the three point correlation function

$$C_{F_j}(r, t_2, t_0, \mathbf{x}, t_1) = \langle\Omega|\mathcal{O}(\mathbf{x}, t_2; \mathbf{y}, t_2)F^2_j(\mathbf{z}, t_1)\mathcal{O}(\mathbf{x}, t_0; \mathbf{y}, t_0)|\Omega\rangle\,. \tag{3.10}$$

In a calculation similar to the one sketched in section 3 but a bit more involved we can derive an expression for ΔF^2_j. For the detailed derivation I refer to my Bachelor thesis [48]. This leads to

$$\Delta F^2_j(r, \mathbf{x}) = \lim_{t_2-t_1, t_1-t_0\to\infty} \underbrace{\frac{C_{F_j}(r, t_2, t_0; \mathbf{x}, t_1)}{C_{Q\bar{Q}}(\mathbf{x}, \mathbf{y}, t_0, t_2)} - \langle\Omega|F^2_j|\Omega\rangle}_{\Delta F^2_{\mathrm{eff},j}(r,t_2,t_0;\mathbf{x},t_1)}, \tag{3.11}$$

where $F^2_{\mathrm{eff},j}(r, t_2, t_0; \mathbf{x}, t_1)$ can be evaluated using euclidean lattice path integrals yielding

$$\Delta E_{\mathrm{eff},j}(r, t_2, t_0; \mathbf{x}, t_1) = +\left(\frac{\langle W(r, t_2, t_0)\cdot P_{0j}(\mathbf{x}, t_1)\rangle_U}{\langle W(r, t_2, t_0)\rangle_U} - \langle P_{0j}\rangle_U\right) \tag{3.12}$$

$$\Delta B_{\mathrm{eff},j}(r, t_2, t_0; \mathbf{x}, t_1) = -\left(\frac{\langle W(r, t_2, t_0)\cdot |\epsilon_{jkl}/2|P_{kl}(\mathbf{x}, t_1)\rangle_U}{\langle W(r, t_2, t_0)\rangle_U} - \langle|\epsilon_{jkl}/2|P_{kl}\rangle_U\right) \tag{3.13}$$

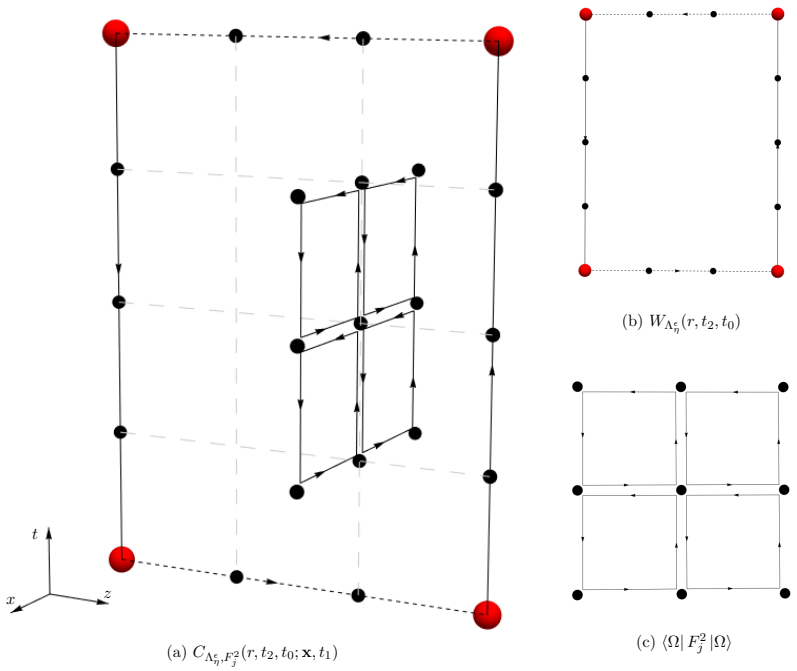

(a) $C_{\Lambda^{\epsilon}_{\eta},F^2_j}(r,t_2,t_0;\mathbf{x},t_1)$ (b) $W_{\Lambda^{\epsilon}_{\eta}}(r,t_2,t_0)$ (c) $\langle\Omega|\, F^2_j\,|\Omega\rangle$

Figure 3.1.: Illustration of equations (3.11) to (3.13) on the lattice. Red spheres, black dots and black arrows represent the quarks, lattice sites and gauge links respectively. Black dashed lines represent operators $a_{\Lambda^{\epsilon}_{\eta}}$. The links in the clover plaquette are shifted for better visibility. Grey dashed lines parallel to the coordinate axes are drawn to guide the eye. (a) $C_{\Lambda^{\epsilon}_{\eta},F^2_j}(r,t_2,t_0;\mathbf{x},t_1)$ for exemplary values $r = 3a$, $t_2 = t_0 + 4a$, $t_1 = (t_2 - t_0)/2$, $\mathbf{x} = \mathbf{n} + 2a\hat{\mathbf{z}}$, and $F_j = E_x$, where $\mathbf{n}$ is the lattice site on which $C_{\Lambda^{\epsilon}_{\eta},F^2_j}$ is evaluated. (b) The corresponding Wilson loop with insertions. (c) The clover plaquette.

with $\langle ... \rangle_U$ denoting the path integral expectation value with integration over link configurations. The different sign for the E_j components results from time ordering.

For the three-point-correlation function in eqs. (3.12) and (3.13) we need to compute the value of the plaquette at lattice space time point $(\mathbf{x}, t)$. On a finite lattice the plaquette $P_{\mu\nu}(\mathbf{x}, t)$ is an object with area $a \cdot a$ in the μ-ν-plane. Similar to the lattice representation of derivatives by the forward derivative, $P_{\mu\nu}(\mathbf{x}, t)$ is not a symmetric discretization. To make computations of the different components of $\Delta F_j^2(r, \mathbf{x})$ more comparable while also reducing lattice artifacts, we introduce a symmetric version of the plaquette

$$P'_{\mu\nu}(\mathbf{x},t) = \frac{1}{4}\left[P_{\mu\nu}(\mathbf{x},t) + P_{\mu\nu}((\mathbf{x},t) - a\hat{\nu}) + P_{\mu\nu}((\mathbf{x},t) - a\hat{\mu}) + P_{\mu\nu}((\mathbf{x},t) - a\hat{\nu} - a\hat{\mu})\right]. \tag{3.14}$$

We note that $\lim_{a\to 0} P'(\mathbf{x}, t) = \lim_{a\to 0} P(\mathbf{x}, t)$, making $P'(\mathbf{x}, t)$ an equivalent quantity in the continuum. This symmetric form of the plaquette is also referred to as "clover leaf". An illustration of eq. (3.11) with this discretization of the plaquette is shown in Figure 3.1.

4. Hybrid static potentials

4.1. Hybrid static potential quantum numbers

Hybrid static potentials are static potentials of quark-antiquark pairs with additional contributions to the quantum numbers by gluonic excitations. As shown in chapter 3 the static potential can be computed by evaluating the Wilson loop on the lattice where the spatial position of temporal links corresponds to the quark position. The ordinary static potential is created by the simplest case of a straight line between the charge positions.
However, there is also the possibility to choose more complex spatial paths which will lead to additional contributions to the quantum numbers. These contributions are determined by the path of gauge links, which are elements of the gauge group SU(3), and thus are gluonic contributions. We will call the part of the Wilson line, which is not a straight path of links along the separation axis *insertion*. The quantum numbers for hybrid static potentials are sketched in Figure 4.1:

- Total angular momentum with respect to the separation axis z:
  $\Lambda \in \{\Sigma \doteq 0, \Pi \doteq 1, \Delta \doteq 2, ..\}$
- The combination of parity and charge conjugation ($P \circ C$):
  $\eta \in \{g \doteq +, u \doteq -\}$
- The spatial reflection along an axis perpendicular to z (P_x):
  $\epsilon \in \{+, -\}$

A state with quantum numbers Λ, η und ϵ will be labeled with Λ_η^ϵ according to the convention. Note that for angular momentum $\Lambda \geq 1$ the energy spectrum is degenerate with respect to ϵ. Therefore we will write Λ_η in this case. As further discussed in section 4.1.4 the shape of the flux tube on the other hand does depend on ϵ. In the following we will derive how to create operators which yield hybrid static potential quantum numbers. For this purpose we define

$$S(\mathbf{x}, \mathbf{y}) = U_\nu(\mathbf{x}) \cdot U_\mu(\mathbf{x} + a\hat{e}_\nu) \cdot ... \cdot U_\rho(\mathbf{y} - a\hat{e}_\rho) \tag{4.1}$$

as an arbitrary spatial path of links starting at $\mathbf{x}$ and ending at $\mathbf{y}$.

4.1.1. Angular momentum

Acting with hybrid static potential creation operators on the vacuum we obtain trial states

$$|\Psi_{hybrid}\rangle_{S;\lambda} = \int_0^{2\pi} d\varphi e^{i\lambda\varphi} R(\phi) \mathcal{O}_S(\mathbf{x}, t; \mathbf{y}, t) |\Omega\rangle , \tag{4.2}$$

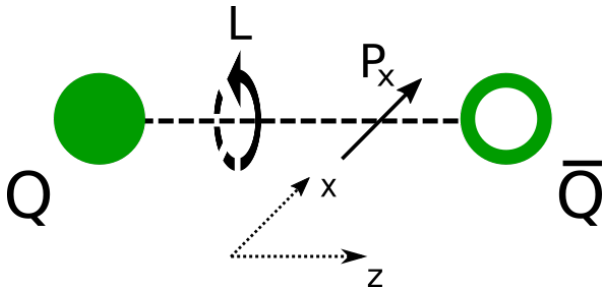

Figure 4.1.: Graphical illustration of hybrid static potential quantum numbers.

where $|\Omega\rangle$ is the vacuum, λ the angular momentum and $R(\varphi)$ denotes a rotation by an angle of φ with respect to the z-axis. Additionally, the operator from eq. (3.1) becomes now

$$\mathcal{O}_S(-r/2, r/2) = \bar{Q}(-r/2) S_z(-r/2, r_1) S(r_1, r_2) S_z(r_2, r/2) Q(r/2) \,|\Omega\rangle\,, \tag{4.3}$$

where the quark and antiquark are at spatial positions (0,0,r/2) and (0,0,-r/2) respectively. On a cubic lattice only rotations by $k \cdot \frac{\pi}{2}, k \in \mathbb{N}$ are possible without changing the shape of the operator

$$|\Psi_{hybrid}\rangle_{S;\lambda} = \sum_{k=0}^{3} \exp\left(\frac{i\pi\lambda k}{2}\right) R\left(\frac{\pi k}{2}\right) \mathcal{O}_S(\mathbf{x}, t; \mathbf{y}, t) \,|\Omega\rangle\,. \tag{4.4}$$

The rotation R of the operator only affects the insertion $S(r_1, r_2)$ from eq (4.2) which is shown in Figure 4.2 (a)-(d). Now the factors of the rotated insertions for the sum in eq. (4.4) can be determined explicitly for a given angular momentum quantum number

$$|\Psi_{hybrid}\rangle_{S;0} = \left[1 + R\left(\frac{\pi}{2}\right) + R\left(\pi\right) + R\left(\frac{3\pi}{2}\right)\right] \mathcal{O}_S(\mathbf{x}, t; \mathbf{y}, t) \,|\Omega\rangle\,, \tag{4.5}$$

$$|\Psi_{hybrid}\rangle_{S;\pm1} = \left[1 \pm iR\left(\frac{\pi}{2}\right) - R\left(\pi\right) \mp iR\left(\frac{3\pi}{2}\right)\right] \mathcal{O}_S(\mathbf{x}, t; \mathbf{y}, t) \,|\Omega\rangle\,, \tag{4.6}$$

$$|\Psi_{hybrid}\rangle_{S;\pm2} = \left[1 - R\left(\frac{\pi}{2}\right) + R\left(\pi\right) - R\left(\frac{3\pi}{2}\right)\right] \mathcal{O}_S(\mathbf{x}, t; \mathbf{y}, t) \,|\Omega\rangle\,. \tag{4.7}$$

Since we consider the total angular momentum quantum number the sign is not a degree of freedom. For even $\Lambda = |\lambda|$ the prefactors are the same anyways but for $\Lambda = 1$ we are left with a choice. Instead of just deciding for either the factors of $\lambda = +1$ or $\lambda = -1$ we take a look at the superposition

$$\frac{1}{2}\left(|\Psi_{hybrid}\rangle_{S;+1} + |\Psi_{hybrid}\rangle_{S;-1}\right) = \left[1 - R\left(\pi\right)\right] \mathcal{O}_S(\mathbf{x}, t; \mathbf{y}, t) \,|\Omega\rangle\,, \tag{4.8}$$

$$\frac{1}{2}\left(|\Psi_{hybrid}\rangle_{S;+1} - |\Psi_{hybrid}\rangle_{S;-1}\right) = \left[iR\left(\frac{\pi}{2}\right) - iR\left(\frac{3\pi}{2}\right)\right] \mathcal{O}_S(\mathbf{x}, t; \mathbf{y}, t) \,|\Omega\rangle\,, \tag{4.9}$$

and immediately notice, that two rotations of the insertion vanish. Thus to simplify computations we choose eq. (4.8) to construct trial states for $\Lambda = 1$.

Since we are restricted to cubic rotations on the lattice the trial states we can construct will also contain contributions from an infinite number of states with higher angular momentum. If we take a look at eq. (4.4) and plug in $\lambda > 2$ we note that trial states for

- $\Lambda = 0$ also receive contributions from $\Lambda = 4k, k \in \mathbb{N}$,
- $\Lambda = 1$ also receive contributions from $\Lambda = 1 + 2k, k \in \mathbb{N}$ and
- $\Lambda = 2$ also receive contributions from $\Lambda = 2 + 4k, k \in \mathbb{N}$.

In practice, anyhow, these higher Λ states will be exponentially suppressed for $t \to \infty$. It would be possible to construct operators with a larger overlap to higher angular momentum states by taking next-to-nearest neighbors on the lattice into account. However, this would be very costly in computation time and is thus not further investigated in this work.

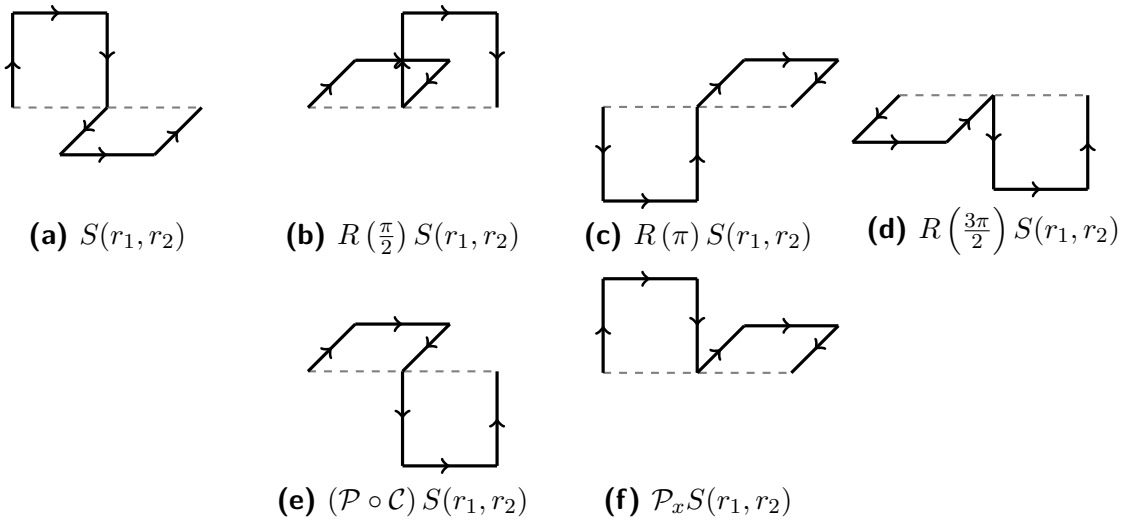

Figure 4.2.: Example for an insertion $S(r_1, r_2)$, its cubic rotations around the z-axis ((a) - (d)) and its behavior under parity and charge conjugation $(\mathcal{P} \circ \mathcal{C})$ (e) as well as under reflection along the x-axis $\mathcal{P}_x$ (f).

4.1.2. Parity and charge conjugation and behavior under spatial reflection

Applying first a charge conjugation and then a parity transformation to eq. (4.3) yields

$$\begin{aligned}(\mathcal{P} \circ \mathcal{C}) \left[\bar{Q}(-r/2) S_z(-r/2, r_1) S(r_1, r_2) S_z(r_2, r/2) Q(r/2)\right] |\Omega\rangle \\ = \bar{Q}(-r/2) S_z(-r/2, -r_2) S_{\mathcal{P}\circ\mathcal{C}}(-r_2, -r_1) S_z(-r_1, r/2) Q(r/2) |\Omega\rangle\,, \quad (4.10)\end{aligned}$$

which is shown in detail in [49]. $S_{\mathcal{P}\circ\mathcal{C}}(-r_2, -r_1)$ is the charge conjugated spatial reflection of $S(r_1, r_2)$ with respect to $(0, 0, 0)^T$.
When reflecting the state from eq. (4.3) at the separation axis along the x-direction we obtain

$$\begin{aligned}\mathcal{P}_x \left[\bar{Q}(-r/2) S_z(-r/2, r_1) S(r_1, r_2) S_z(r_2, r/2) Q(r/2)\right] |\Omega\rangle \\ = \bar{Q}(-r/2) S_z(-r/2, -r_2) S_{\mathcal{P}_x}(r_1, r_2) S_z(-r_1, r/2) Q(r/2) |\Omega\rangle\,, \quad (4.11)\end{aligned}$$

where $S_{\mathcal{P}_x}(r_1, r_2)$ is $S(r_1, r_2)$ reflected at the separation axis along the x-direction.
Both $S_{\mathcal{P}\circ\mathcal{C}}(-r_2, -r_1)$ and $S_{\mathcal{P}_x}(r_1, r_2)$ are shown for an exemplary insertion in Figure 4.2 (e) and (f).

4.1.3. Constructing trial states and correlation functions

We need to take into account all combinations of shapes we obtain by applying $R(\pi)$, $(\mathcal{P}\circ\mathcal{C})$ and $\mathcal{P}_x$ to an insertion $S(r_1,r_2)$ with the weight of the corresponding quantum numbers. Consequently, we can write a trial state for a hybrid static potential with quantum numbers Λ_η^ϵ as

$$\begin{aligned}|\Psi_{S;\Lambda_\eta^\epsilon}\rangle &= \frac{1}{4}\left(1+\eta\,(\mathcal{P}\circ\mathcal{C})+\epsilon\,\mathcal{P}_x+\eta\,\epsilon\,(\mathcal{P}\circ\mathcal{C})\,\mathcal{P}_x\right)\sum_{k=0}^{3}\exp\left(\frac{i\pi\Lambda k}{2}\right)R\left(\frac{\pi k}{2}\right)\mathcal{O}_S\,|\Omega\rangle \\ &= \bar{Q}(-r/2)\alpha_{S,\Lambda_\eta^\epsilon}(-r/2,r/2)Q(r/2)\,|\Omega\rangle\,. \end{aligned} \tag{4.12}$$

where

$$\begin{aligned}&\alpha_{S,\Lambda_\eta^\epsilon}(-r/2,r/2) = \\ &\quad= \frac{1}{4}\sum_{k=0}^{3}\exp\left(\frac{i\pi\Lambda k}{2}\right)R\left(\frac{\pi k}{2}\right)\Big[U(-r/2,r_1)\left(S(r_1,r_2)+\epsilon\,S_{\mathcal{P}_x}(r_1,r_2)\right)U(r_2,r/2)+ \\ &\quad+U(-r/2,-r_2)\left(\eta\,S_{(\mathcal{P}\circ\mathcal{C})}(-r_2,-r_1)+\eta\,\epsilon\,S_{(\mathcal{P}\circ\mathcal{C})\mathcal{P}_x}(-r_2,-r_1)\right)U(-r_1,r/2)\Big].\end{aligned} \tag{4.13}$$

This gives a total of $4\cdot 2\cdot 2 = 16$ spatial paths that need to be computed. In most of the cases some of these paths are identical though, e.g. if we take a look at the insertion from Figure 4.2 we will quickly notice that the sum over the rotations of $(\mathcal{P}\circ\mathcal{C})\,S(r_1,r_2)$ and $\mathcal{P}_x S(r_1,r_2)$ as well as the sum over the rotations of $S(r_1,r_2)$ and $(\mathcal{P}\circ\mathcal{C})\,\mathcal{P}_x S(r_1,r_2)$ will be the same, leading to only 8 different paths in total.
We also note that not every operator $S(r_1,r_2)$ can be used to construct trial states for any given Λ_η^ϵ since eq. (4.12) can become zero. We can also infer from eq. (4.12) that even though the potential is degenerate with respect to ϵ for $\Lambda \geq 1$ the correlation functions are different from each other. The insertions $S(r_1,r_2)$ used in this work are the optimal choices, i.e. have the highest overlap with the ground state for separations $r=6$ and $r=10$ as determined in [26]. They are described in detail in Figure 4.3.

Analogously to section 3 we can now write down the correlation function for a hybrid static potential trial state

$$C_{Q\bar{Q},\Lambda_\eta^\epsilon} = \langle\Psi_{S;\Lambda_\eta^\epsilon}|\Psi_{S;\Lambda_\eta^\epsilon}\rangle \underset{t_2-t_0\to\infty}{\propto} \exp\left(V_{\Lambda_\eta^\epsilon}(t_2-t_0)\right), \tag{4.14}$$

and consequently obtain a modified version of the Wilson loop

$$\begin{aligned}&\tilde{W}(r,t_2,t_0) = \\ &\quad= \mathrm{Tr}\left[\alpha_{S,\Lambda_\eta^\epsilon}(-r/2,r/2,t_0)U(r/2;t_0,t_2)\left(\alpha_{S,\Lambda_\eta^\epsilon}(-r/2,r/2,t_2)\right)^\dagger U(-r/2;t_2,t_0)\right].\end{aligned} \tag{4.15}$$

Correspondingly we just need to replace the ordinary Wilson loop in eqs. (3.12) and (3.13) to compute the field strength components for hybrid static potentials.

$US_{\mathrm{III},1}U = U_x^2 U_y^2 U_z^{E_z} U_{-y}^2 U_{-x}^2$

Σ_g^-

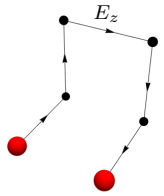

r/a	6	10
E_z	6	10

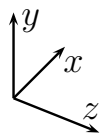

$US_{\mathrm{III},4}U = U_x^4 U_y^2 U_z^{E_z} U_{-y}^2 U_{-x}^4 U_z^{E_z}$

Σ_u^+

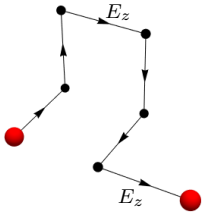

r/a	6	10
E_z	3	5

$US_{\mathrm{I},3}U = U_x^5 U_z^{E_z} U_{-x}^{E_{x,1}} U_z U_{-x}^{E_{x,2}} U_z$

Δ_g^+

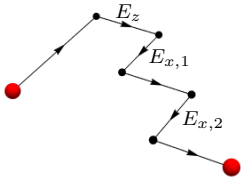

r/a	6	10
E_z	4	8
$E_{x,1}$	2	3
$E_{x,2}$	3	2

$US_{\mathrm{V},1}U = U_z^{E_{z,1}} U_x^3 U_y^3 U_z^{E_{z,2}} U_{-x}^3 U_{-y}^3 U_z^{E_{z,1}}$

Σ_u^-

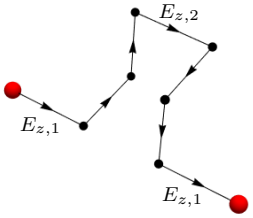

r/a	6	10
$E_{z,1}$	1	2
$E_{z,2}$	4	6

$US_{\mathrm{I},3}U = U_x^{E_{x,1}} U_z^5 U_{-x}^{E_{x,2}} U_z^{E_z} U_{-x}^{E_{x,3}} U_z^{E_{z,3}}$

Δ_u^+

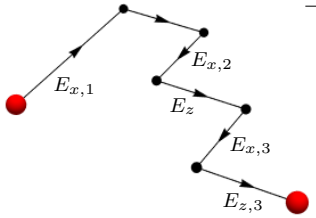

r/a	6	10
$E_{x,1}$	4	5
$E_{x,2}$	2	5
E_z	1	0
$E_{x,3}$	2	0
$E_{z,3}$	0	5

$US_{\mathrm{I},3}U = U_x^{E_x} U_z^{E_z} U_{-x}^{E_x} U_z$

Π_g^-

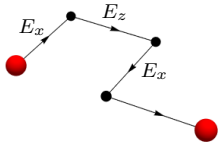

r/a	6	10
E_x	3	2
E_z	5	9

$US_{\mathrm{III},1}U = U_x U_y^4 U_z^{E_z} U_{-y}^4 U_{-x}$

Δ_g^-

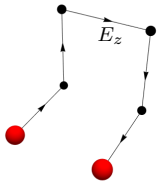

r/a	6	10
E_z	6	10

$US_{\mathrm{III},1}U = U_x U_y^3 U_z^{E_z} U_{-y}^3 U_{-x}$

Π_u^+

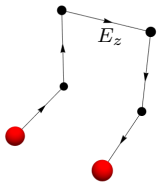

r/a	6	10
E_z	6	10

$US_{\mathrm{III},3}U = U_x^2 U_y^2 U_z^{E_{z,1}} U_{-y}^2 U_z^{E_{z,2}} U_{-x}^2$

Δ_u^-

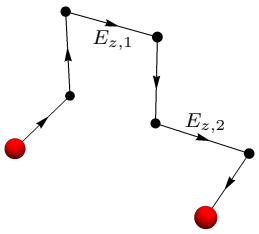

r/a	6	10
$E_{z,1}$	5	8
$E_{z,2}$	1	2

Figure 4.3.: Optimized creation operators for $\Lambda_\eta^\epsilon = \Sigma_g^-, \Sigma_u^+, \Sigma_u^-, \Pi_g, \Pi_u, \Delta_g, \Delta_u$. The notation is analogous to [26] and explained in detail there. For $\Pi_\eta^\pm$ we obtain $\Pi_\eta^\mp$ by the transformation in 4.34 to 4.36. For Δ_η^ϵ we need to do separate computations for both $\epsilon = +$ and $\epsilon = -$.

4.1.4. Angular dependence of $\Delta F_j^2(r, \mathbf{x})$

As already mentioned in section 4.1 computing the static quark-antiquark potential $V_{\Lambda_\eta^\epsilon}(r)$ yields results independent of ϵ for $\Lambda \geq 1$. However, the flux densities $\Delta F^2_{j,\Lambda_\eta^\epsilon}(r, \mathbf{x})$ are not independent of this quantum number. In the following we will show that $\Delta F^2_{j,\Lambda_\eta^+}(r, \mathbf{x})$ and $\Delta F^2_{j,\Lambda_\eta^-}(r, \mathbf{x})$ are related by rotations around the separation axis and construct an observable $\Delta F^2_{j,\Lambda_\eta}(r, \mathbf{x})$ which is independent of ϵ.
To this end, we consider

$$\langle O_{\Lambda_\eta^\pm}(r)|\hat{R}_z^\dagger(\alpha)F_j^2(\mathbf{x})\hat{R}_z(\alpha)|O_{\Lambda_\eta^\pm}\rangle - \langle\Omega|F_j^2|\Omega\rangle \tag{4.16}$$

where the rotation operator $\hat{R}_z(\alpha)$ can be expressed in matrix representation as

$$R(\alpha) = \begin{pmatrix} +c_\alpha & -s_\alpha & 0 \\ +s_\alpha & +c_\alpha & 0 \\ 0 & 0 & 1 \end{pmatrix}. \tag{4.17}$$

where we introduced $c_\alpha = \cos(\alpha)$ and $s_\alpha = \sin(\alpha)$ which will be used throughout this chapter. By applying $\hat{R}_z(\alpha)$ on the one hand to the operator $F_j^2(\mathbf{x})$ and on the other hand to the states $|O_{\Lambda_\eta^\pm}(r)\rangle$ we will be able to find a relation between $\Delta F^2_{j,\Lambda_\eta^\epsilon}(r, R(-\alpha)\mathbf{x})$ and $\Delta F^2_{j,\Lambda_\eta^\epsilon}(r, \mathbf{x})$.
The field strength components transform as

$$\hat{R}_z^\dagger(\alpha)F_j^a(\mathbf{x})\hat{R}_z(\alpha) = R_{jk}(-\alpha)F_k^a(R(-\alpha)\mathbf{x}) = R_{jk}(-\alpha)F_k^a(\mathbf{x}_{-\alpha}) \tag{4.18}$$

where $\mathbf{x}_{-\alpha} = R(-\alpha)\mathbf{x}$. This leads to

$$\begin{aligned}
&\langle O_{\Lambda_\eta^\pm}(r)|\hat{R}_z^\dagger(\alpha)F_j^2(\mathbf{x})\hat{R}_z(\alpha)|O_{\Lambda_\eta^\pm}\rangle - \langle\Omega|F_j^2|\Omega\rangle = \\
&= \langle O_{\Lambda_\eta^\pm}(r)|(R_{jk}(-\alpha)F_k(\,\mathbf{x}_{-\alpha}))^2|O_{\Lambda_\eta^\pm}\rangle - \langle\Omega|F_j^2|\Omega\rangle \\
&= \begin{pmatrix} c_\alpha^2\Delta F^2_{x,\Lambda_\eta^\pm}(r,\mathbf{x}_{-\alpha}) + s_\alpha^2\Delta F^2_{y,\Lambda_\eta^\pm}(r,\mathbf{x}_{-\alpha}) + 2c_\alpha s_\alpha \langle O_{\Lambda_\eta^\pm}(r)|F_x^2(\mathbf{x}_{-\alpha})F_y^2(\mathbf{x}_{-\alpha})|O_{\Lambda_\eta^\pm}(r)\rangle \\ c_\alpha^2\Delta F^2_{y,\Lambda_\eta^\pm}(r,\mathbf{x}_{-\alpha}) + s_\alpha^2\Delta F^2_{x,\Lambda_\eta^\pm}(r,\mathbf{x}_{-\alpha}) - 2c_\alpha s_\alpha \langle O_{\Lambda_\eta^\pm}(r)|F_x^2(\mathbf{x}_{-\alpha})F_y^2(\mathbf{x}_{-\alpha})|O_{\Lambda_\eta^\pm}(r)\rangle \\ \Delta F^2_{z,\Lambda_\eta^\pm}(r,\mathbf{x}_{-\alpha}) \end{pmatrix}_j,
\end{aligned} \tag{4.19}$$

where we used that $\langle\Omega|F_j^2|\Omega\rangle = \langle\Omega|F_k^2|\Omega\rangle$ for all $j, k \in \{1, 2, 3\}$ to expand

$$\langle\Omega|F_j^2|\Omega\rangle = c_\alpha^2\langle\Omega|F_j^2|\Omega\rangle + s_\alpha^2\langle\Omega|F_k^2|\Omega\rangle = c_\alpha^2\langle\Omega|F_k^2|\Omega\rangle + s_\alpha^2\langle\Omega|F_j^2|\Omega\rangle. \tag{4.20}$$

Static potential eigenstates $|O_{\lambda_\eta}(r)\rangle$ where $\Lambda = |\lambda|$ are also eigenstates of the z-component of the angular momentum operator $\hat{J}_z$

$$\hat{R}_z(\alpha)\,|O_{\lambda_\eta}(r)\rangle = e^{i\alpha\hat{J}_z}\,|O_{\lambda_\eta}(r)\rangle = e^{i\alpha\lambda}\,|O_{\lambda_\eta}(r)\rangle. \tag{4.21}$$

Now we consider the rotation of a $\mathcal{P}_x$-transformed state

$$\begin{aligned}
\hat{R}_z(\alpha)\left(\mathcal{P}_x\,|O_{\lambda_\eta}(r)\rangle\right) = e^{i\alpha\hat{J}_z}\mathcal{P}_x\,|O_{\lambda_\eta}(r)\rangle &= \mathcal{P}_x e^{i(-\alpha)\hat{J}_z}\,|O_{\lambda_\eta}(r)\rangle \\
&= e^{i(-\alpha)\lambda}\left(\mathcal{P}_x\,|O_{\lambda_\eta}(r)\rangle\right),
\end{aligned} \tag{4.22}$$

where we used that $\hat{J}_z\mathcal{P}_x = -\mathcal{P}_x\hat{J}_z$ and also note that

$$\mathcal{P}_x \left|O_{+\lambda_\eta}(r)\right\rangle = \left|O_{-\lambda_\eta}(r)\right\rangle . \tag{4.23}$$

This allows us to relate $|O_{\pm\lambda_\eta}(r)\rangle$ to $|O_{\Lambda^\epsilon_\eta}(r)\rangle$ as

$$\left|O_{\Lambda^\pm_\eta}(r)\right\rangle = \frac{1}{\sqrt{2}}\left(\left|O_{+\lambda_\eta}(r)\right\rangle \pm \left|O_{-\lambda_\eta}(r)\right\rangle\right). \tag{4.24}$$

By using eq. (4.21) and rewriting the exponential functions with trigonometric ones we obtain

$$\hat{R}_z(\alpha)\left|O_{\Lambda^\pm_\eta}(r)\right\rangle = c_{\alpha\Lambda}\left|O_{\Lambda^\pm_\eta}(r)\right\rangle + is_{\alpha\Lambda}\left|O_{\Lambda^\mp_\eta}(r)\right\rangle . \tag{4.25}$$

Plugging eq. (4.25) into eq. (4.16) yields

$$\begin{aligned}\langle O_{\Lambda^\pm_\eta}(r)|\hat{R}^\dagger_z(\alpha)F^2_j(\mathbf{x})\hat{R}_z(\alpha)|O_{\Lambda^\pm_\eta}\rangle - \langle\Omega|F^2_j|\Omega\rangle = \\ = c^2_{\alpha\Lambda}\Delta F^2_{j,\Lambda^\pm_\eta}(r;\mathbf{x}) + s^2_{\alpha\Lambda}F^2_{j,\Lambda^\mp_\eta}(r;\mathbf{x}) + ic_{\alpha\Lambda}s_{\alpha\Lambda}\left(\langle O_{\Lambda^\pm_\eta}(r)|F^2_j(\mathbf{x})|O_{\Lambda^\mp_\eta}(r)\rangle\right).\end{aligned} \tag{4.26}$$

Now we can equate eqs. (4.19) and (4.26) to obtain a relation between $\Delta F^2_{j,\Lambda^\pm_\eta}(r;\mathbf{x})$ and $\Delta F^2_{j,\Lambda^\pm_\eta}(r;\mathbf{x}_{-\alpha})$. We note that the rotation operation does not leave $\Delta F^2_{j,\Lambda^\pm_\eta}(r;\mathbf{x})$ invariant for $\Lambda \geq 1$ while for $\Lambda = 0$ it does.
The choice of ϵ as a quantum number is not unique, one can also fully describe hybrid static potential states by the set of quantum numbers λ_η where $\lambda \in -2,-1,0,1,2$. The potentials are still degenerate with respect to the newly introduced sign of λ ($V_{-\lambda_\eta} = V_{+\lambda_\eta}$). If we apply the rotation transformation upon states in this representation we obtain for the transformed operator essentially eq. (4.19) with the replacement $\Lambda^\epsilon_\eta \to \lambda_\eta$, while the states transform much more simple according to eq. (4.21). This means the behavior of the static potential field densities under rotation and consequently the field strength components themselves is different depending on the set of quantum numbers we choose to describe the system. Since V_{Λ_η} is fully characterized by Λ and η we want to remove this angular dependence, which is just arising due to the (to some extend) arbitrary choice of this third quantum number. To this end, we define

$$\Delta F^2_{j,\Lambda_\eta}(r,\mathbf{x}) = \frac{1}{2}\left(\Delta F^2_{j,\Lambda^+_\eta}(r,\mathbf{x}) + \Delta F^2_{j,\Lambda^-_\eta}(r,\mathbf{x})\right) = \frac{1}{2}\mathrm{Tr}\left[\mathcal{P}_{\Lambda_\eta}\left(F^2_j(\mathbf{x}) - \langle\Omega|F^2_j|\Omega\rangle\right)\right] \tag{4.27}$$

where the projection operator

$$\mathcal{P}_{\Lambda_\eta} = \left|O_{\Lambda^+_\eta}(r)\right\rangle\left\langle O_{\Lambda^+_\eta}(r)\right| + \left|O_{\Lambda^-_\eta}(r)\right\rangle\left\langle O_{\Lambda^\pm_\eta}(r)\right| \tag{4.28}$$

shows explicitly, that $\Delta F^2_{j,\Lambda_\eta}(r,\mathbf{x})$ is independent of the basis used to span the space introduced by ϵ or the sign of λ.
Performing the rotation using $\Delta F^2_{j,\Lambda_\eta}(r,\mathbf{x})$ yields

$$\begin{aligned}&\Delta F^2_{j,\Lambda_\eta}(r,\mathbf{x}) = \\ &= \begin{pmatrix} c^2_\alpha\Delta F^2_{x,\Lambda_\eta}(r,\mathbf{x}_{-\alpha}) + s^2_\alpha\Delta F^2_{y,\Lambda_\eta}(r,\mathbf{x}_{-\alpha}) + \sum_\epsilon c_\alpha s_\alpha\left\langle O_{\Lambda^\pm_\eta}(r)|F^2_x(\mathbf{x}_{-\alpha})F^2_y(\mathbf{x}_{-\alpha})|O_{\Lambda^\pm_\eta}(r)\right\rangle \\ c^2_\alpha\Delta F^2_{y,\Lambda^\pm_\eta}(r,\mathbf{x}_{-\alpha}) + s^2_\alpha\Delta F^2_{x,\Lambda^\pm_\eta}(r,\mathbf{x}_{-\alpha}) - \sum_\epsilon c_\alpha s_\alpha\left\langle O_{\Lambda^\pm_\eta}(r)|F^2_x(\mathbf{x}_{-\alpha})F^2_y(\mathbf{x}_{-\alpha})|O_{\Lambda^\pm_\eta}(r)\right\rangle \\ \Delta F^2_{z,\Lambda^\pm_\eta}(r,\mathbf{x}_{-\alpha}) \end{pmatrix}_j .\end{aligned} \tag{4.29}$$

We immediately notice that the z-component is now left invariant under this transformation, while the other components still change. However, we can define

$$\Delta F^2_{\perp,\Lambda_\eta}(r,\mathbf{x}_{-\alpha}) = \frac{1}{2}\left(\Delta F^2_{x,\Lambda_\eta}(r,\mathbf{x}_{-\alpha}) + \Delta F^2_{y,\Lambda_\eta}(r,\mathbf{x}_{-\alpha})\right) \tag{4.30}$$

which is also invariant under rotations around the separation axis.

If we consider rotations by an angle α which is a multiple of $\frac{\pi}{2}$ (cubic rotations) the mixed terms in eqs. (4.19) and (4.26) will vanish. This yields

$$\Delta F^2_{x,\Lambda^\pm_\eta}(r,(x,y,z)^T) = \Delta F^2_{y,\Lambda^\pm_\eta}(r,(\pm y,\mp x,z)^T) \tag{4.31}$$
$$\Delta F^2_{y,\Lambda^\pm_\eta}(r,(x,y,z)^T) = \Delta F^2_{x,\Lambda^\pm_\eta}(r,(\pm y,\mp x,z)^T) \tag{4.32}$$
$$\Delta F^2_{z,\Lambda^\pm_\eta}(r,(x,y,z)^T) = \Delta F^2_{z,\Lambda^\pm_\eta}(r,(\pm y,\mp x,z)^T) \tag{4.33}$$

for $\Lambda = \Sigma, \Delta$ and

$$\Delta F^2_{x,\Pi^\pm_\eta}(r,(x,y,z)^T) = \Delta F^2_{y,\Pi^\mp_\eta}(r,(\pm y,\mp x,z)^T) \tag{4.34}$$
$$\Delta F^2_{y,\Pi^\pm_\eta}(r,(x,y,z)^T) = \Delta F^2_{x,\Pi^\mp_\eta}(r,(\pm y,\mp x,z)^T) \tag{4.35}$$
$$\Delta F^2_{z,\Pi^\pm_\eta}(r,(x,y,z)^T) = \Delta F^2_{z,\Pi^\mp_\eta}(r,(\pm y,\mp x,z)^T) \tag{4.36}$$

for $\Lambda = \Pi$. These equations can be explicitly used to test and improve results from the lattice by averaging over field densities related by this symmetry.

5. Results

Some of the results in this work were obtained in collaboration with Christian Reisinger. In particular, he generated and provided the SU(3) configurations.

5.1. Lattice setup

All numerical results in this work are obtained using SU(2) and SU(3) lattice gauge theory. In both cases the standard Wilson lattice gauge action was used to create gauge configurations.

The SU(2) gauge configurations were obtained using a standard heatbath algorithm. Auto-correlation of subsequent configurations was kept minimal by using a binning of 100 heatbath sweeps. For the heatbath simulation we generated 48 000 configurations with $\beta = 2.5$, which corresponds to a lattice spacing of $a = 0.079$ fm when identifying r_0 with 0.5 fm and a lattice volume $(L/a)^3 \times (T/a) = 24^4$. In some earlier simulations a setup of 13 000 configurations on a lattice with $(L/a)^3 \times (T/a) = 18^4$ and the same β was used, which will be referred to when discussing finite volume effects in section 5.2.2.

The SU(3) gauge configurations were obtained using the Chroma QCD library [50]. Each update sweep comprises a heatbath and four relaxation steps and configurations are separated by 20 of these sweeps. In this case we generated 5500 configurations and used $\beta = 6.0$ which corresponds to a lattice spacing of $a = 0.093$fm with the same identification of r_0. The lattice volume is $(L/a)^3 = 24^3$ and $(T/a) = 48$.

To improve the signal-to-noise-ratio several types of smearing techniques were used for the computation of Wilson loops:

- Spatial gauge links on the lattice are APE-smeared links (see the detailed discussion in [51]). The smearing parameters $\alpha_{APE} = 0.5$ and $N_{APE} = 20$ were chosen in a way to create large overlaps to the ground state (optimized in [26]).
- For some simulations HYP2-smeared gauge links are used [52–54], improving the statistical errors significantly by reducing the self energy of the static quarks. This however comes with the cost of very large discretization errors for small r and $\mathbf{x}$ near the quark positions. There is a more detailed discussion in section 5.2.3.

We perform a plateau fit of $\Delta F_{\text{eff},j}(r, t_2, t_0; \mathbf{x}, t_1)$ in a suitable range determined by a χ^2 minimization. Statistical errors shown in this work are obtained by a standard jackknife analysis [55] of this fit.

5.2. Systematic errors

5.2.1. Plateaus of $F^2_{\mathbf{eff},j}(r, t_2, t_0; \mathbf{x}, t_1)$

Our computations yield results for $F^2_{\mathrm{eff},j}(r, t_2, t_0; \mathbf{x}, t_1)$ according to 3.12 and 3.13. As expressed in 3.11 we will find convergence of the effective field densities for sufficiently high $(t_2-t_1)/a$ and $(t_1-t_0)/a$. To this end we computed the field densities for temporal extents of the Wilson loop $(t_2-t_0)/a \in 0, 1, ..., 10$ where $t_1 = (t_2-t_0)/2$ for even $(t_2-t_0)/a$ and $t_1 = (t_2 - t_0 + a)/2$ for odd $(t_2 - t_0)/a$.

We fit a constant using an uncorrelated χ^2 minimization in the range of $t_{\min} \leq t_2 - t_0 \leq t_{\max}$ where we chose a $t_{\max}$ for which the signal does not completely vanish in noise. Data points for higher values of $t_{\max}$ do not contribute to the fit because of very large errors. Since the convergence of $F^2_{\mathrm{eff},j}(r, t_2, t_0; \mathbf{x}, t_1)$ should not depend on $\mathbf{x}$ we want to find $t_{\min}$ such that $\chi^2/\mathrm{N_{dof}} \lesssim 1$ is valid for all spatial lattice points $\mathbf{x}$. We also need to keep in mind that the fit will naturally be better for values $F^2_{\mathrm{eff},j}(r, t_2, t_0; \mathbf{x}, t_1) \approx 0$ which would spoil the results in the $t_{\min}$-optimization considerably. We define $\tilde{\mathbf{x}}$ as the lattice points where $F^2_{\mathrm{eff},j}(r, t_2, t_0; \mathbf{x}, t_1) \not\approx 0$ and $N_{\tilde{\mathbf{x}}}$ as the number of those points. Now we find a $t_{\min}$ such that

$$\frac{1}{N_{\tilde{\mathbf{x}}}} \sum_{\tilde{\mathbf{x}}} \chi^2(\tilde{\mathbf{x}})/\mathrm{N_{dof}} \lesssim 1. \tag{5.1}$$

The ordinary static potential shows significantly lower errors. Additionally the results from HYP-smeared configurations have a considerably better signal-to-noise ratio. The optimized values $t_{\min}$ and $t_{\max}$ for all investigated sectors Λ^ϵ_η are shown in the following table:

	$t_{\min}[a]$	$t_{\max}[a]$	$t_{\min,\mathrm{HYP}}[a]$	$t_{\max,\mathrm{HYP}}[a]$
Σ^+_g	5	9	6	10
Σ^-_g	3	5	3	8
Σ^+_u	3	5	3	7
Σ^-_u	3	6	4	9
Π_g	3	6	3	8
Π_u	3	7	4	10
Δ_g	3	6	4	8
Δ_u	3	5	3	7

Table 5.1.: Optimized $t_{\min}$ and $t_{\max}$ by χ^2 - minimization for sectors $\Lambda^\epsilon_\eta = \Sigma^-_g, \Sigma^+_u, \Sigma^-_u, \Pi_g, \Pi_u, \Delta_g, \Delta_u$ with unsmeared $\tilde{W}$ and HYP2-smeared $\tilde{W}$.

In figure 5.1 we show $F^2_{\mathrm{eff},j}(r, t_2, t_0; \mathbf{x}, t_1)$ for the 8 investigated sectors Λ^ϵ_η and corresponding fitted plateaus.

To further check for contributions of higher states, one can in principle consider different insertions than the ones shown in 4.3. In the limit of sufficiently high $t_2 - t_0$ the flux densities are independent of the creation operator since only the ground state will remain.
We find consistency of our results with computations of different operators for Π_u and Δ_g at an earlier stage of this work (see [46]).

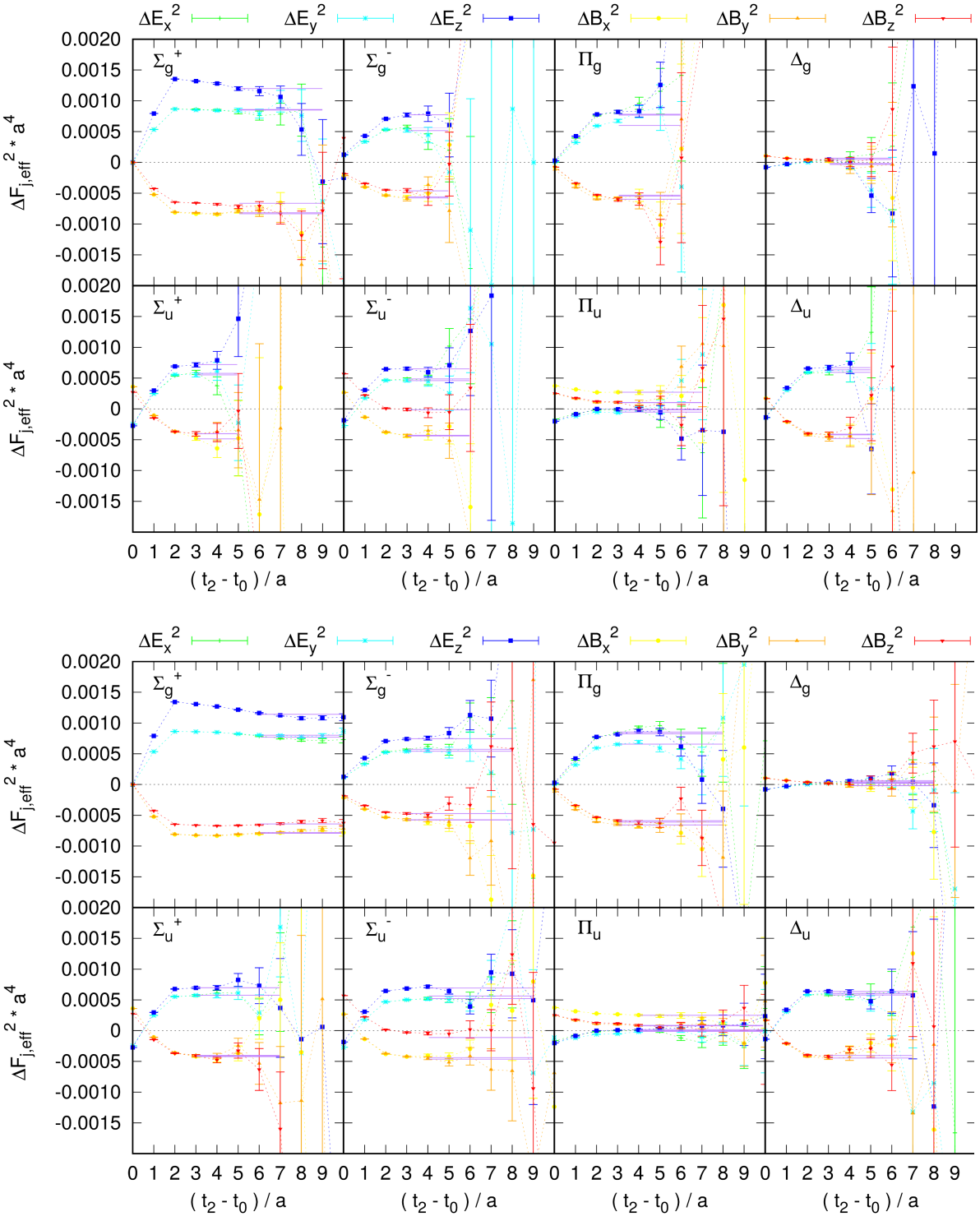

Figure 5.1.: $\Delta F^2_{\mathrm{eff},j}(r, t_2, t_0; \mathbf{x}, t_1)$ as a function of temporal separation of the Wilson loop $t_2 - t_0$ for gauge group SU(2), $\Lambda^\epsilon_\eta = \Sigma^-_g, \Sigma^+_u, \Sigma^-_u, \Pi_g, \Pi_u, \Delta_g, \Delta_u$ and $Q\bar{Q}$ - separation $r = 10a$. Ranges of the plateau fits $[t_{min}, t_{max}]$ are indicated with purple lines.
Top: $\tilde{W}$ is computed with unsmeared temporal links
Bottom: $\tilde{W}$ is computed with HYP2-smeared temporal links

5.2.2. Discretization errors and finite volume effects

From studies of the ordinary static potential flux tubes large discretization errors are expected for small $Q\bar{Q}$ - separations r $= |\mathbf{r}_Q - \mathbf{r}_{\bar{Q}}| \leq 3a$ or measurements of the field densities near the quark positions, i.e. $F_j^2(r, \mathbf{x})$ with $|\mathbf{x} - \mathbf{r}_Q| \leq 2a$ or $|\mathbf{x} - \mathbf{r}_{\bar{Q}}| \leq 2a$. These effects will get a larger radius when performing HYP2-smearing as discussed in the next chapter.
We only have results for one lattice spacing a and thus cannot make any statements regarding the continuum limit.

It is known, that finite volume effects for static potentials with $Q\bar{Q}$ - separation $r < R/2$ where R denotes the spatial lattice extent are rather small. Additionally we consider pure gauge theory where the lightest particle, the $J^{PC} = 0^{++}$ glueball, is already very heavy, i. e. where $m_{\text{glueball}} \cdot L > 3000$.
We performed simulations on a 18^4 lattice with a smaller sample size, which are consistent with our main results.

5.2.3. HYP2-smearing of temporal links

We observed that using HYP2-smearing on temporal links for the computation of $\tilde{W}$ reduces the statistical errors by a factor of five to eight. However, at the same time new systematic errors are introduced. In figure 5.2 we show the flux densities for $\Lambda_\eta^\epsilon = \Sigma_g^+, \Sigma_u^-$ and $Q\bar{Q}$ - separation $r = 10a$ on the separation axis with and without HYP2-smearing. We observe a strong suppression of the peak-like structure at the charge positions for $\Delta F_j^2(r, \mathbf{x})$ for HYP-smeared Wilson loops. This is not an unexpected behavior:

The spatial position of the time links in the Wilson loop correspond to the quark and antiquark position. Due to the discretization they do not represent point charges but rather can be interpreted as spherical (color) charges with radii $a/2$. HYP2-smearing on temporal links can then essentially be considered as replacing the link by a so called fat link of width $2a$ which effectively increases the charges' radii to $3a/2$.
Without HYP-smearing the extension of the charge distribution is small enough that we still observe peaks at the quark and antiquark position. After HYP2-smearing the charge extension becomes large enough that we now measure $\Delta F_j^2(r, \mathbf{x})$ inside the charge distribution. As we already know from classical electrostatics, the field strength inside a homogeneously charged volume is proportional to ρ, i. e. a hole, instead of $\frac{1}{\rho^2}$, i. e. a peak, for a point-like charge where ρ is the distance to the center of the charge distribution.

From figure 5.2 we can infer that discrepancies between unsmeared and HYP2-smeared results are

- large for $|\mathbf{x} - \mathbf{r}_Q| \leq a$
- negligible within statistical errors for
  - $|\mathbf{x} - \mathbf{r}_Q| \geq 4a$ when $\Delta F_j^2(r, \mathbf{x}) = \Delta E_z^2(r, \mathbf{x})$ and
  - $|\mathbf{x} - \mathbf{r}_Q| \geq 3a$ for all other components

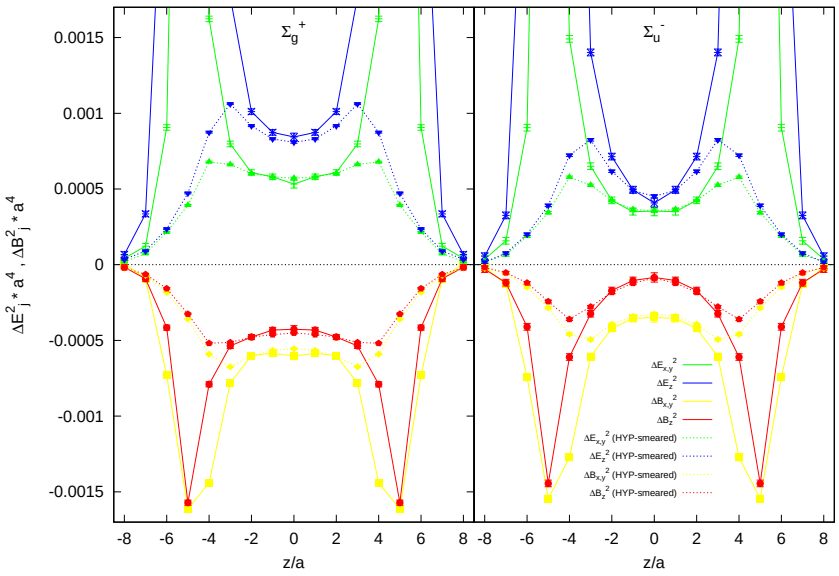

Figure 5.2.: $\Delta F_j^2(r, \mathbf{x})$ on the separation plane $\mathbf{x} = (0, 0, z)^T$ for gauge group SU(3), $\Lambda_\eta^\epsilon = \Sigma_g^-, \Sigma_u^+$ and $Q\bar{Q}$ - separation $r = 10a$.

Consequently we will not use HYP2-smearing for computations of the field densities in the separation plane (w.l.o.g. x-z-plane with $y = 0$).
On the mediator plane on the other hand (the x-y-plane with $z = 0$) we have the best agreement of HYP-smeared and HYP-unsmeared $\Delta F_j^2(r, \mathbf{x})$. In figure 5.3 we show both at $\mathbf{x} = (0, 0, 0)^T$ for different $Q\bar{Q}$-separations r for $\Lambda_\eta^\epsilon = \Sigma_g^+, \Sigma_u^-$. We find agreement if

- $r \geq 10$ for $\Delta E_z^2(r, \mathbf{x} = (x, y, 0)^T)$ in the case of $\Lambda_\eta^\epsilon = \Sigma_g^+$,
- $r \geq 8$ for $\Delta E_z^2(r, \mathbf{x} = (x, y, 0)^T)$ in the case of all other Λ_η^ϵ sectors,
- $r \geq 6$ for all other components of $\Delta F_j^2(r, \mathbf{x} = (x, y, 0)^T)$.

As a consequence we perform computations on the mediator axis with HYP2-smearing and primarily show results for $Q\bar{Q}$ - separation $r = 10a$ in 5.3.2.

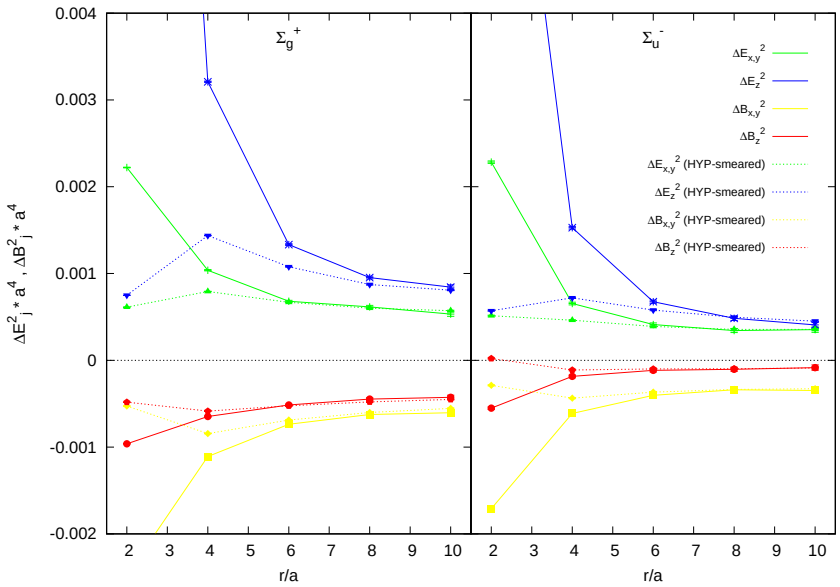

Figure 5.3.: $\Delta F_j^2(r, \mathbf{x})$ as a function of r at $\mathbf{x} = (0,0,0)^T$ for gauge group SU(3), $\Lambda_\eta^\epsilon = \Sigma_g^-, \Sigma_u^+$ and $Q\bar{Q}$ - separation $r = 10a$.

5.3. Hybrid static potential flux densities

We performed identical computations in both SU(2) and SU(3) lattice gauge theory. There appear to be no differences within statistical errors. Consequently we opted to only show results from the gauge group SU(2) in this section due to better statistics, while we refer to the appendix for the SU(3)-version of the plots (see A).

5.3.1. Symmetrization of flux densities

To reduce the statistical errors as much as possible we averaged over flux densities related by symmetries which give explicit constraints for the flux density structure. These are

- reflection at all three planes parametrized by $(x, y, 0)^T$, $(x, 0, z)^T$ and $(0, y, z)^T$ and
- behavior under rotation as discussed in section 4.1.4 given by eqs. (4.31) to (4.36).

First of all we checked that our results are consistent with these symmetries and then we used them to reduce statistical errors by averaging over flux densities related by them. We show the field strength components for Π_u^+, Π_u^- and Δ_u^+, Δ_u^- on the mediator plane in the upper row of Figure 5.4 and 5.5 respectively. The results for Π_u^- did not require additional simulations since according to eqs. (4.34) to (4.36) we can transform one into the other by a cubic rotation of $\frac{\pi}{2}$. This is not possible for $\Lambda = \Delta$ though since Δ_η^+ and Δ_η^- are related by rotations of $\frac{\pi}{4}$ as one can see in Figure 5.5 and thus we computed both Δ_η^+ and Δ_η^- separately.

In the lower part of figure 5.4 and 5.5 we determined $\Delta F_{j,\Lambda_\eta}^2(r, \mathbf{x})$ according to eq. (4.27) as the average of the flux densities for $\epsilon = +$ and $\epsilon = -$.
In the following only the symmetrized version of the flux densities $\Delta F_{j,\Lambda_\eta}^2(r, \mathbf{x})$ will be shown for $\Lambda \geq 1$.

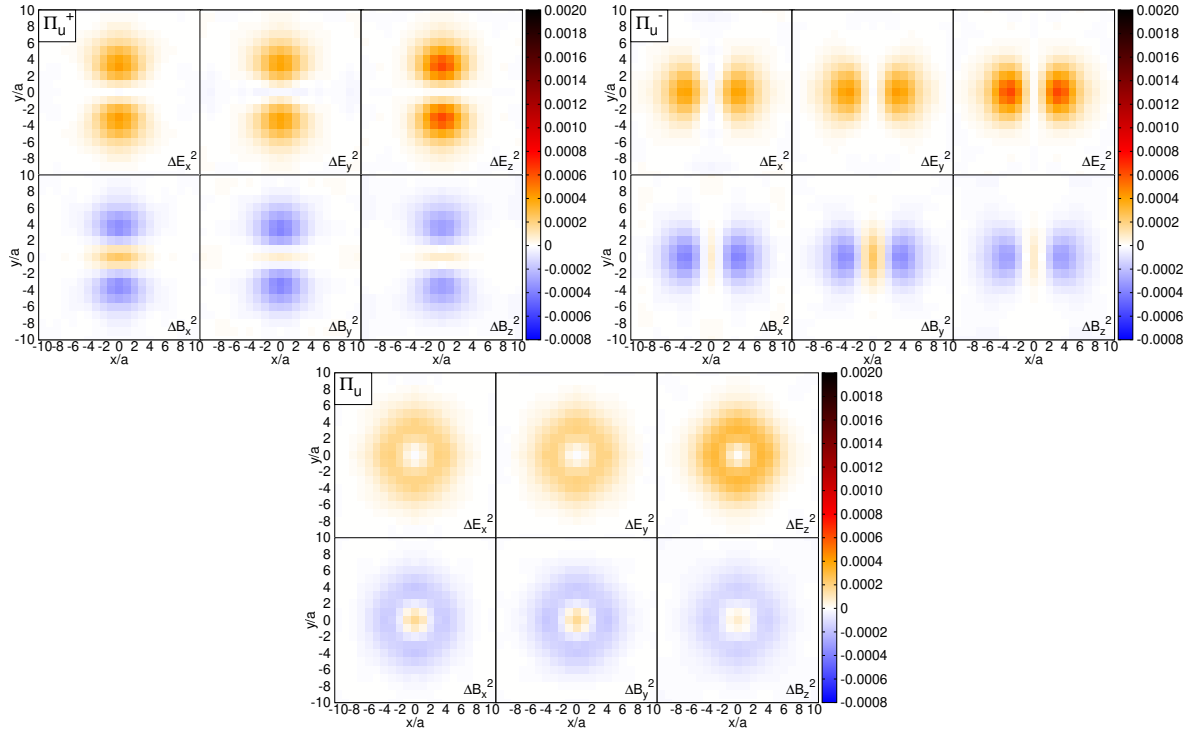

Figure 5.4.: Flux densities $\Delta F^2_{j,\Pi_u^+}(r,\mathbf{x})$, $\Delta F^2_{j,\Pi_u^-}(r,\mathbf{x})$ and $\Delta F^2_{j,\Pi_u}(r,\mathbf{x})$ in the mediator plane for gauge group SU(2) and $Q\bar{Q}$ - separation $r = 10a$

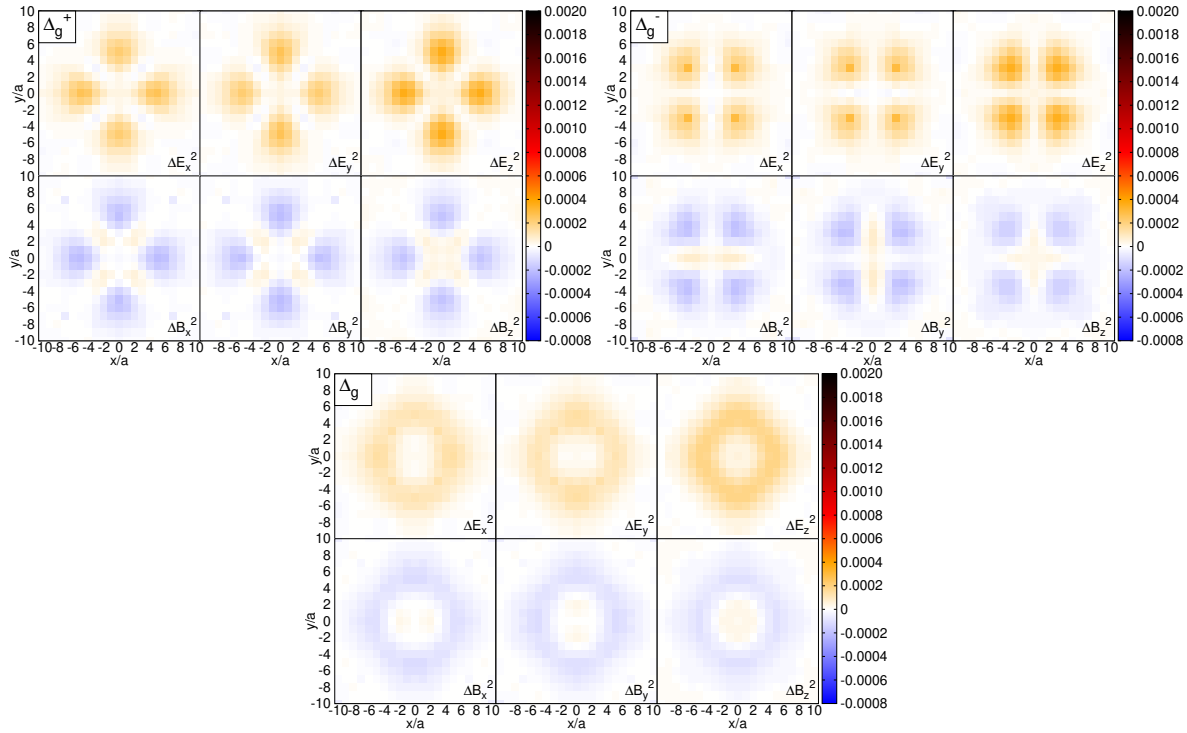

Figure 5.5.: Flux densities $\Delta F^2_{j,\Delta_g^+}(r,\mathbf{x})$, $\Delta F^2_{j,\Delta_g^-}(r,\mathbf{x})$ and $\Delta F^2_{j,\Delta_g}(r,\mathbf{x})$ in the mediator plane for gauge group SU(2) and $Q\bar{Q}$ - separation $r = 10a$

5.3.2. Flux densities on the mediator plane

In this section we show results for the flux tube structure on the mediator plane. As discussed in section 5.2.3 we used HYP-smearing in this region, resulting in better signal-to-noise ratio compared to measurements on the separation plane which will be discussed in the next chapter.
In Figure 5.6 and 5.7 we show all squared field strength components $\Delta F^2_{j,\Lambda_\eta^{(\epsilon)}}(r,\mathbf{x})$ for $Q\bar{Q}$-separations $r = 6a$ and $r = 10a$ for all sectors $\Lambda_\eta^{(\epsilon)}$ in the form of 2D color maps. As discussed in section 5.2.3 HYP2-smearing introduces systematic errors for $r = 6a$. Consequently, we should consider the left side of Figure 5.6 and 5.7 more as a crude qualitative result what happens for smaller separations and the right side as the main results. In the upper panel of Figure 5.8 flux densities on a mediator axis are plotted, using $\Delta F^2_{\perp,\Lambda_\eta^{(\epsilon)}}(r,\mathbf{x})$ and $\Delta F^2_{z,\Lambda_\eta^{(\epsilon)}}(r,\mathbf{x})$ which are invariant under rotations around the z-axis. In contrast to the 2D color maps these curves have the advantage, that they allow us to provide information about the precision of our numerical results. The statistical errors become larger as the ground state energy $V_{Q\bar{Q},\Lambda_\eta^{(\epsilon)}}(r)$ increases (see Figure 7 in [26] for results of the hybrid static potential $V_{Q\bar{Q},\Lambda_\eta^{(\epsilon)}}(r)$).
In the lower panel of Figure 5.8 we show the difference between hybrid flux densities and the ordinary one by plotting $\Delta F^2_{j,\Lambda_\eta^{(\epsilon)}}(r,\mathbf{x}) - \Delta F^2_{j,\Sigma_g^+}(r,\mathbf{x})$.

5.3.3. Flux densities on the separation plane

In this section we present plots for the flux densities on the separation plane (plane in which the charges are located) for all sectors $\Lambda_\eta^{(\epsilon)} = \Sigma_g^-, \Sigma_u^+, \Sigma_u^-, \Pi_g, \Pi_u, \Delta_g, \Delta_u$ and both $Q\bar{Q}$ - separations $r = 6a$ and $r = 10a$ in the form of 2D color maps in figures 5.9 and 5.10. We refrained from showing curve-like plots on the separation axis, since they only show a very small amount of information. Also note that as discussed in section 5.2.2 flux densities in the vicinity of the charges, i.e. $|\mathbf{x} - \mathbf{r}_Q| \leq 2a$ or $|\mathbf{x} - \mathbf{r}_{\bar{Q}}| \leq 2a$, entail large discretization errors and consequently should be ignored.
Our computations of the flux tubes for the ordinary static $Q\bar{Q}$ - potential yield the well-known cigar-like string structure with the z-components of $\Delta F^2_j(r,\mathbf{x})$ providing the largest contribution to the energy density, the maximum on the separation axis and monotonically decreasing field strength when moving away along a mediator axis.
Hybrid static potential flux tubes on the other hand show a variety of different structures. As prominently visible in the lower panel of 5.8 excited gluons yield an increase in chromomagnetic flux densities near the center of the flux tube. We can also infer from 5.8, 5.9 and 5.10 that flux tubes become wider, i.e. have a larger extension in x- and y-direction.
There are also some properties, that only a certain group of hybrid flux densities have in common. On the one hand we notice a clear reduction of chromoelectric flux density in the center to approximately the vacuum field strength $(\Pi_u, \Delta_g, \Sigma_u^-)$ while for $\Lambda_\eta^\epsilon = \Sigma_u^+, \Pi_g, \Delta_u$ we find a localized peak of chromoelectric field strength represented by a cross-like structure in the 2D-color maps. These peaks in either chromoelectric or chromomagnetic field strength can be interpreted as an explicit gluon. This picture of a so called valence gluon generating hybrid quantum numbers is common, when discussing hybrid mesons in models and phenomenological descriptions. The peaks are surrounded

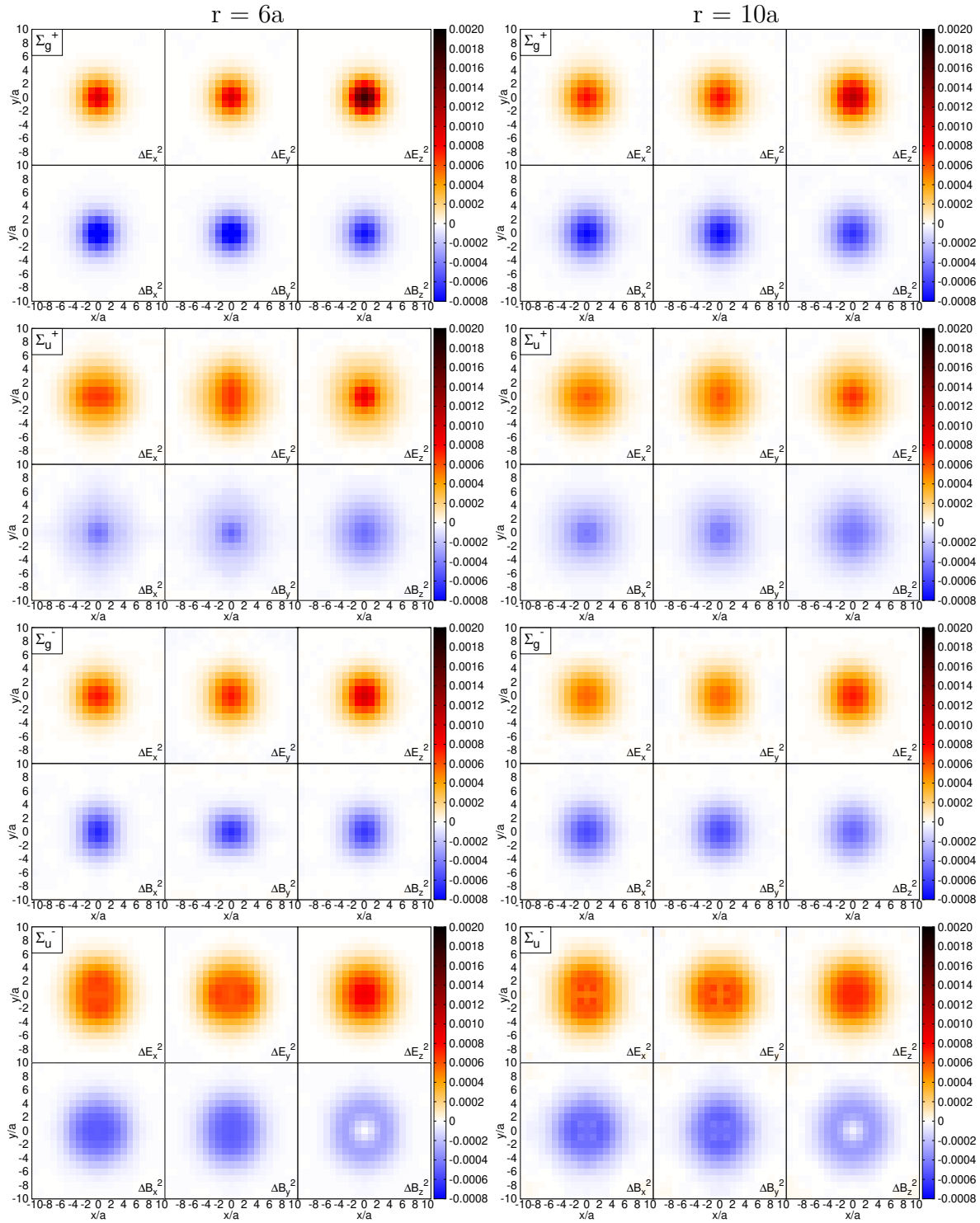

Figure 5.6.: $\Delta F^2_{j,\Lambda_\eta^{(\epsilon)}}(r,\mathbf{x})$ for $\Lambda_\eta^\epsilon = \Sigma_+^g, \Sigma_g^-, \Sigma_u^+, \Sigma_u^-$ on the mediator plane for gauge group SU(2).
Left: $Q\bar{Q}$ - separation $R = 6a$.
Right: $Q\bar{Q}$ - separation $R = 10a$.

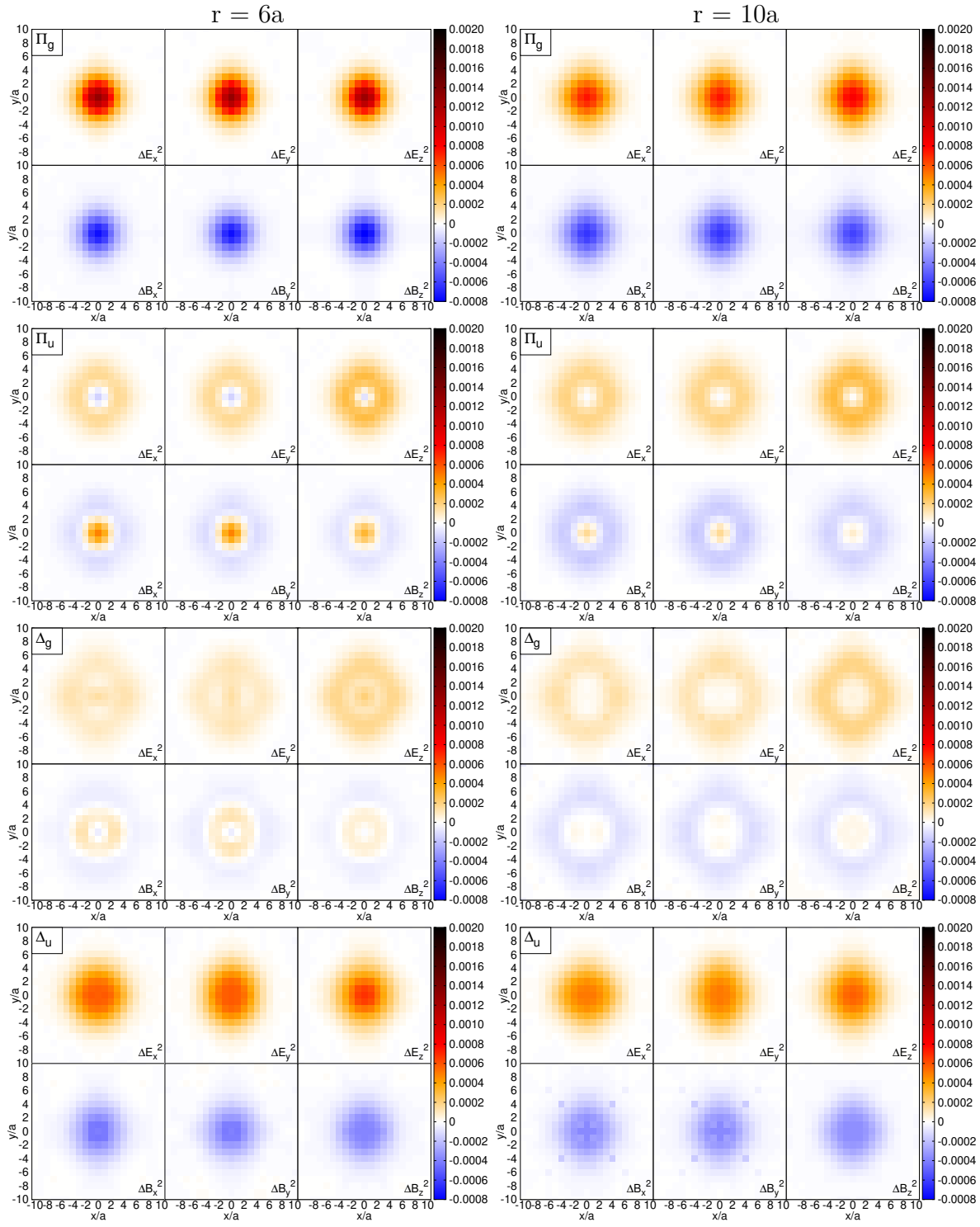

Figure 5.7.: $\Delta F^2_{j,\Lambda^{(\epsilon)}_\eta}(r,\mathbf{x})$ for $\Lambda^\epsilon_\eta = \Pi_g, \Pi_u, \Delta_g, \Delta_u$ on the mediator plane for gauge group SU(2).
Left: $Q\bar{Q}$ - separation $r = 6a$.
Right: $Q\bar{Q}$ - separation $r = 10a$.

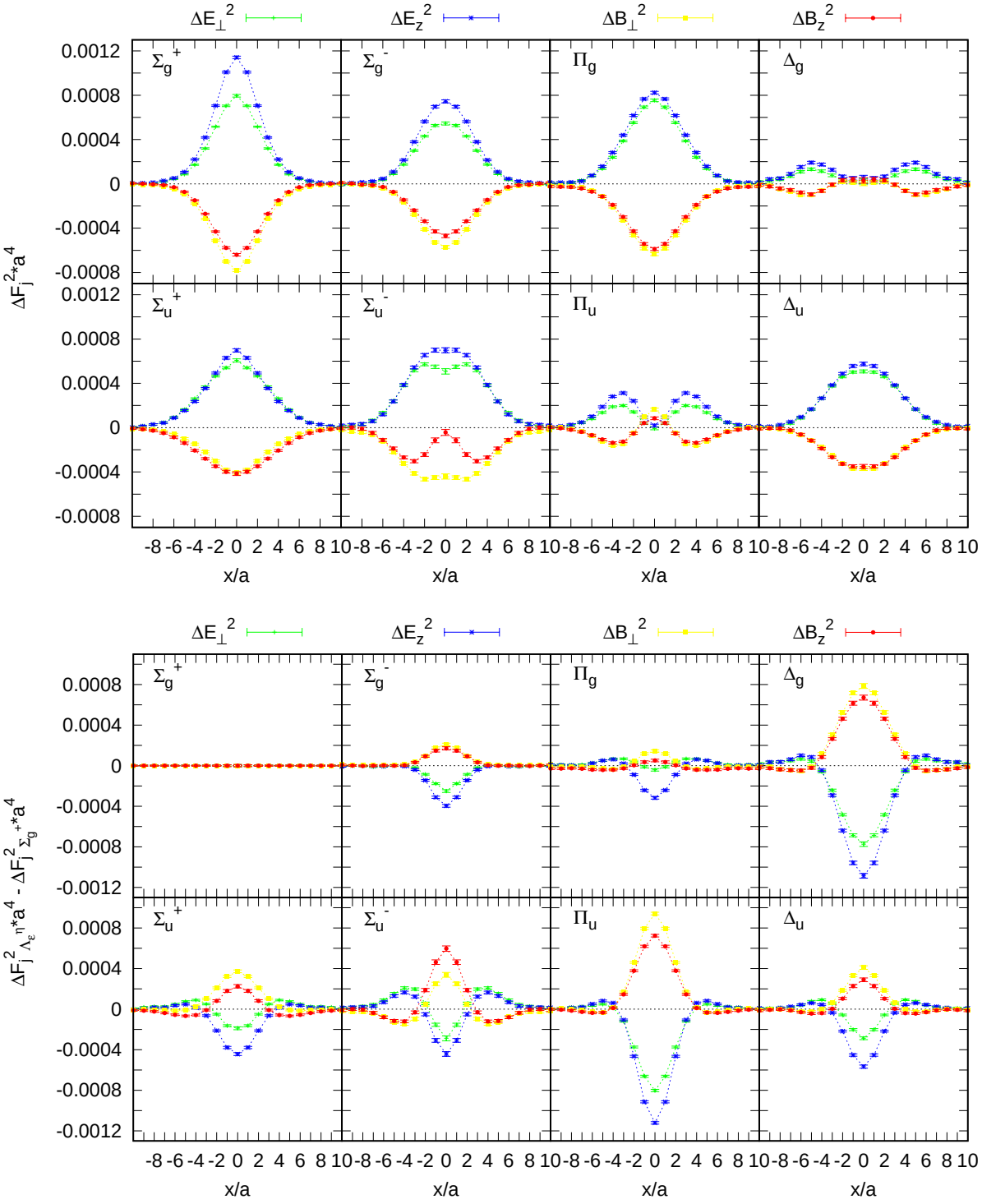

Figure 5.8.: Flux densities on a mediator axis (x-axis) for $\Lambda_\eta^\epsilon = \Sigma_+^g, \Sigma_g^-, \Sigma_u^+, \Sigma_u^- \Pi_g, \Pi_u, \Delta_g, \Delta_u$, gauge group SU(2) and $Q\bar{Q}$ - separation $r = 10a$.
Top: $\Delta F^2_{j,\Lambda_\eta^{(\epsilon)}}(r, \mathbf{x})$ where $j \in \{\perp, z\}$
Bottom: $\Delta F^2_{j,\Lambda_\eta^{(\epsilon)}}(r, \mathbf{x}) - \Delta F^2_{j,\Sigma_g^+}(r, \mathbf{x})$ where $j \in \{\perp, z\}$

by a shell-like spherical structure visible as rings in the 2D color plots from figure 5.9 and 5.10. This gives an indication for vibrating strings, where at $(0,0,0)^T$ there could either be a maximum or a node. The string picture is also consistent with our result for different $Q\bar{Q}$-separations since the transverse extent of the flux tube structure does not change with r.

5.3.4. Comparison to existing works

In potential non-relativistic QCD (pNRQCD) gluonic excitations of a heavy $Q\bar{Q}$ - pair can be realized by a local operator in the center between quark and antiquark (figure 5.11) consisting of field strength components and their covariant derivatives (e.g. [56], [57]). If we only consider the leading order terms in the multipole expansion and set the separation axis to be the z-axis these operators take the simple form showed in table 5.2.

	$\hat{O}(F_j)$	$\hat{O}(D_k F_j)$
Σ_g^+	$1,\ E_z$	
Σ_g^-		$D_z B_z$
Σ_u^+		$D_z E_z$
Σ_u^-	B_z	$D_x E_y - D_y E_x$
Π_g	$E_x,\ E_y$	$D_x B_z - D_z B_x,\ D_y B_z - D_z B_y$
Π_u	$B_x,\ B_y$	$D_x E_z - D_z E_x,\ D_y E_z - D_z E_y$
Δ_g		$D_x B_x - D_y B_y,\ D_x B_y + D_y B_x$
Δ_u		$D_x E_x - D_y E_y,\ D_x E_y + D_y E_x$

Table 5.2.: Gluonic excitation operators at leading order in the multipole expansion of pNRQCD. The separation axis is the z-axis and D_j denotes the covariant derivative.

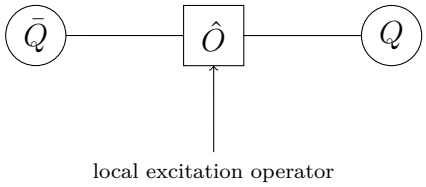

Figure 5.11.: Sketch of an insertion of a local excitation operator to realize hybrid quantum numbers in a heavy $Q\bar{Q}$ - system

Obviously we can not compare results in a quantitative sense but rather need to draw phenomenological parallels. An insertion only containing F_j is expected to enhance this very field strength component which would result in a significant higher contribution of F_j to the energy density compared to the ordinary flux tubes. In Figure 5.8 we can observe exactly this behaviour for $\Lambda_\eta^\epsilon = \Sigma_g^+, \Sigma_u^-, \Pi_g, \Pi_u$.
It is known from lattice gauge theory that derivative operators such as e.g. $D_x E_z - D_z E_x$ for Π_u generate nodes in the corresponding wave functions. This would lead to vanishing field strength components in the center surrounded by maxima which is indeed the case according to our lattice results as indicated by double peaks on the mediator axis in Figure 5.8 lower panel.

Recently there has been another investigation of hybrid flux tubes in SU(3) lattice Yang-Mills-theory [43]. Our results are in fair agreement within statistical errors taking into account that different lattice spacings have been used. While in [43] two hybrid sectors were studied ($\Lambda_\eta^{(\epsilon)} = \Pi_u, \Sigma_u^+$), we computed the flux densities for in total seven hybrid sectors ($\Lambda_\eta^{(\epsilon)} = \Sigma_u^+, \Sigma_g^-, \Sigma_u^-, \Pi_g, \Pi_u, \Delta_g, \Delta_u$) with smaller errors by an factor of up to five.

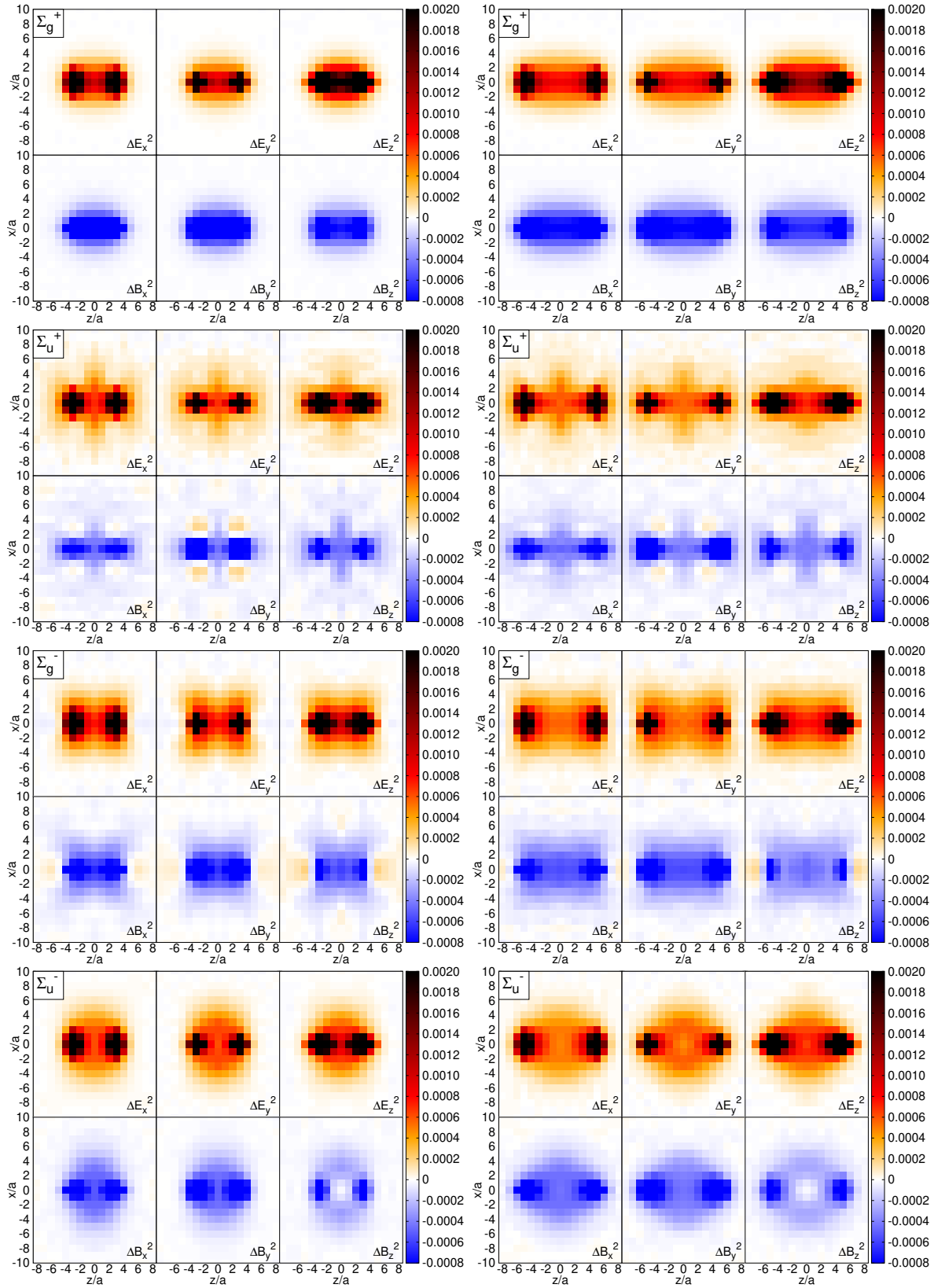

Figure 5.9.: $\Delta F^2_{j,\Lambda^{(\epsilon)}_\eta}(r,\mathbf{x})$ for $\Lambda^\epsilon_\eta = \Sigma^g_+, \Sigma^-_g, \Sigma^+_u, \Sigma^-_u$ on the separation plane for gauge group SU(2).
Left: $Q\bar{Q}$ - separation $R = 6a$.
Right: $Q\bar{Q}$ - separation $R = 10a$.

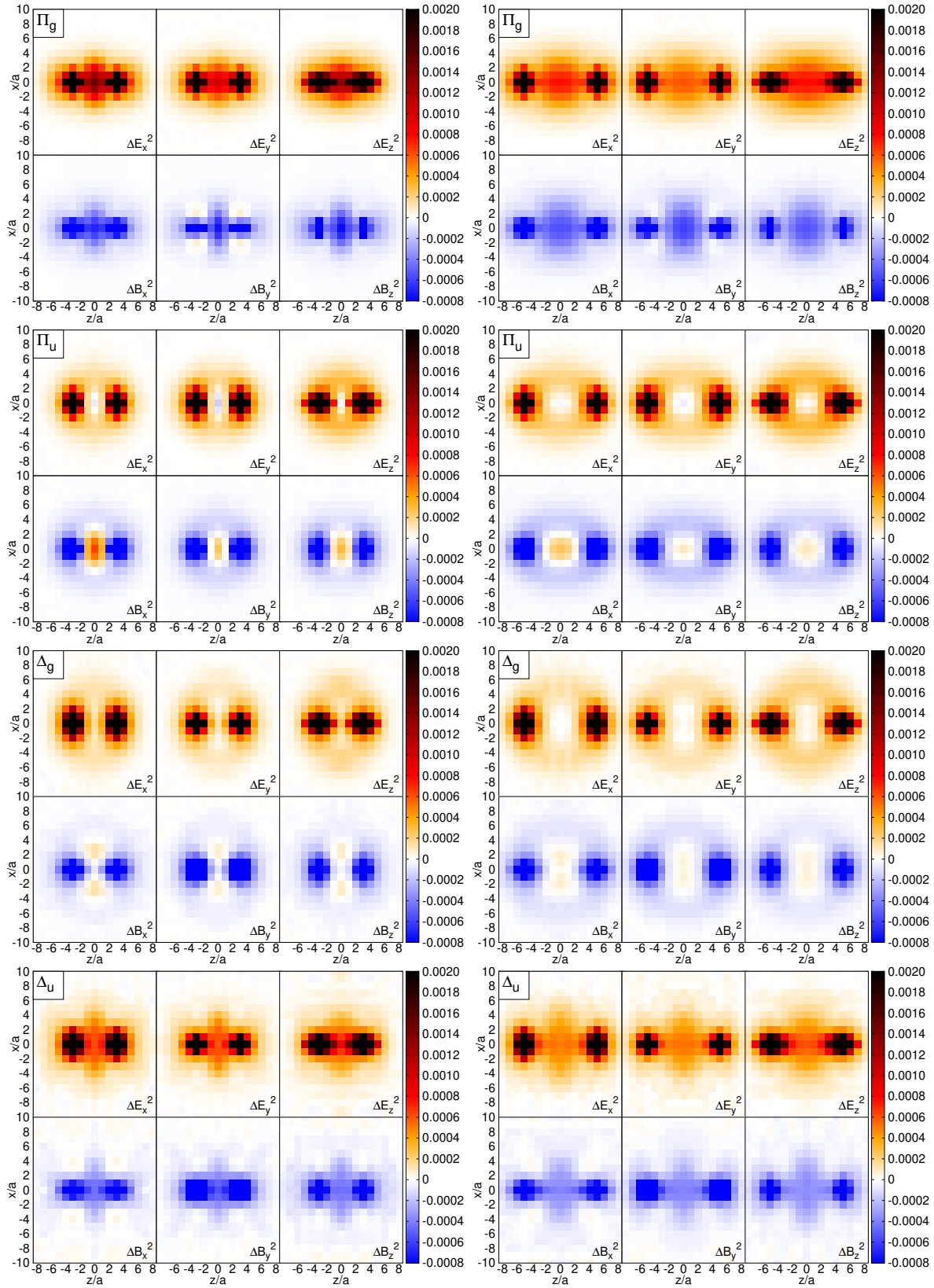

Figure 5.10.: $\Delta F^2_{j,\Lambda_\eta^{(\epsilon)}}(r,\mathbf{x})$ for $\Lambda_\eta^\epsilon = \Pi_g, \Pi_u, \Delta_g, \Delta_u$ on the separation plane for gauge group SU(2).
Left: $Q\bar{Q}$ - separation $r = 6a$.
Right: $Q\bar{Q}$ - separation $r = 10a$.

6. Conclusion and Outlook

We computed the squared field strength components of the ordinary static potential $\Lambda_\eta^{(\epsilon)} = \Sigma_g^+$ and seven hybrid static potentials $\Lambda_\eta^\epsilon = \Sigma_g^-, \Sigma_u^+, \Sigma_u^-, \Pi_g, \Pi_u, \Delta_g, \Delta_u$. To this end we fitted plateaus on the effective flux densities $\Delta F_{\mathrm{eff},j}(r, t_2, t_0; \mathbf{x}, t_1)$ for the limit of large $t_2 - t_0$. We also investigated systematic effects of HYP2-smearing on temporal links and improved our signal-to-noise ratio by using it under certain conditions.

We find agreement with independent lattice studies of other working groups in the hybrid sectors $\Lambda_\eta^{(\epsilon)} = \Pi_u, \Sigma_u^+$ [43] and obtain for the first time results in five more sectors $\Lambda_\eta^{(\epsilon)} = \Sigma_g^-, \Sigma_u^-, \Pi_g, \Delta_g, \Delta_u$.
The distinctive properties of the structure of flux tubes for a given $\Lambda_\eta^{(\epsilon)}$ appear to be expected when comparing to studies of local excitation operators from pNRQCD [56, 57]. Furthermore our numerical results are consistent with a string picture of confinement.

Going forward one could investigate smaller lattice spacings and larger volumes to perform a continuum extrapolation and the infinite volume limit. However, we do not expect much different results since we already computed flux densities for a smaller lattice size [44], finding consistent results, and also addressed discretization errors in the discussion of HYP2-smeared versus unsmeared $\tilde{W}$.

One could also include dynamical fermions into the simulations of two heavy quarks to study not only excitations in the gluon sector but additionally light quark distributions. This would allow a more general study of heavy-heavy exotic mesons rather than only hybrid mesons [15]. Anyhow, this kind of simulations poses to be rather complicated since the system can now just decay into a static potential and one or more light mesons.

A. Flux densities for gauge group SU(3)

We show flux densities for the gauge group SU(3) in Figures A.1 to A.5. These plots are very similar to the corresponding SU(2)-plots in Figures 5.6 to 5.9. You find a detailed discussion in section 5.

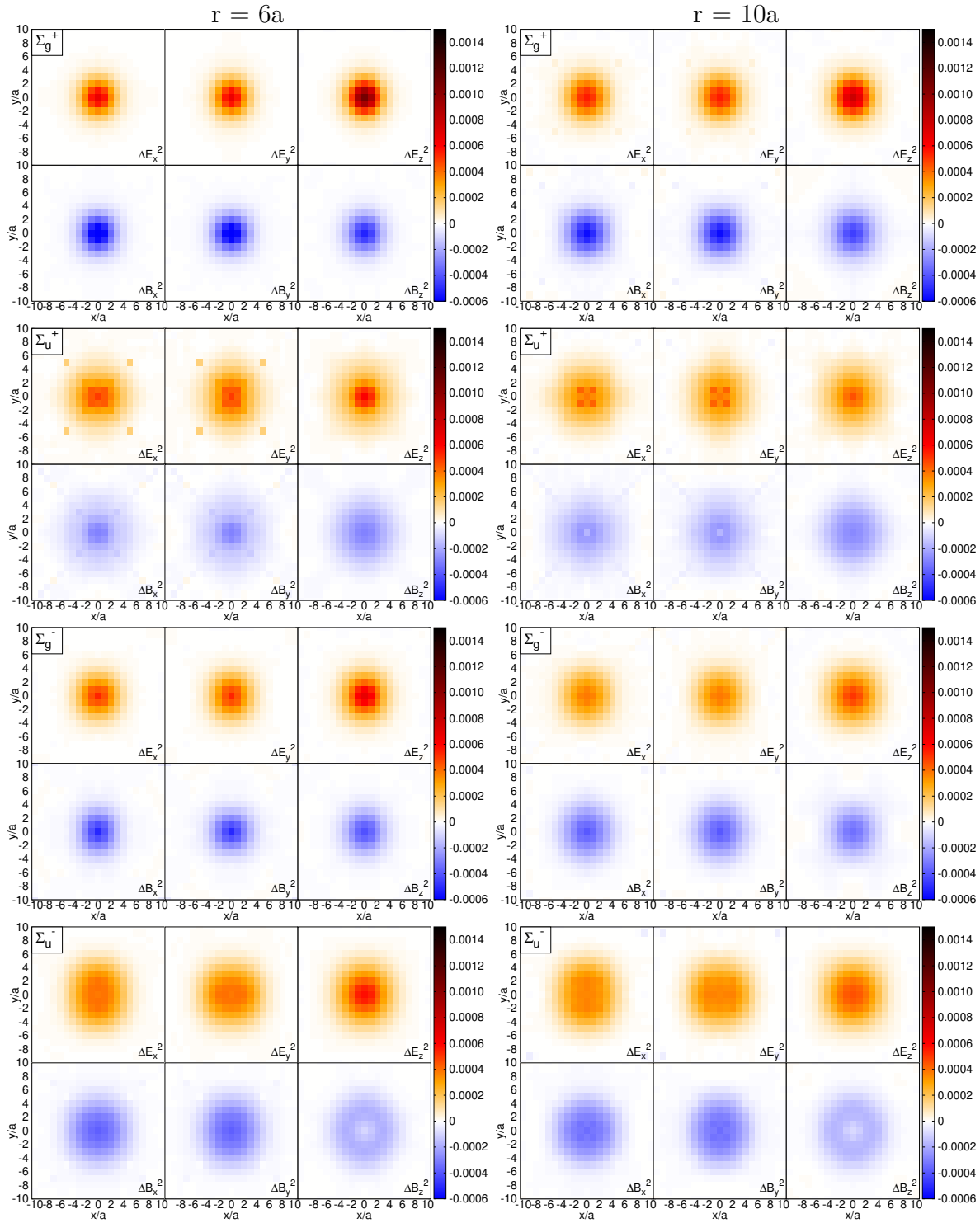

Figure A.1.: $\Delta F^2_{j,\Lambda_\eta^{(\epsilon)}}(r,\mathbf{x})$ for $\Lambda_\eta^\epsilon = \Sigma_+^g, \Sigma_g^-, \Sigma_u^+, \Sigma_u^-$ on the mediator plane for gauge group SU(3).
Left: $Q\bar{Q}$ - separation $R = 6a$.
Right: $Q\bar{Q}$ - separation $R = 10a$.

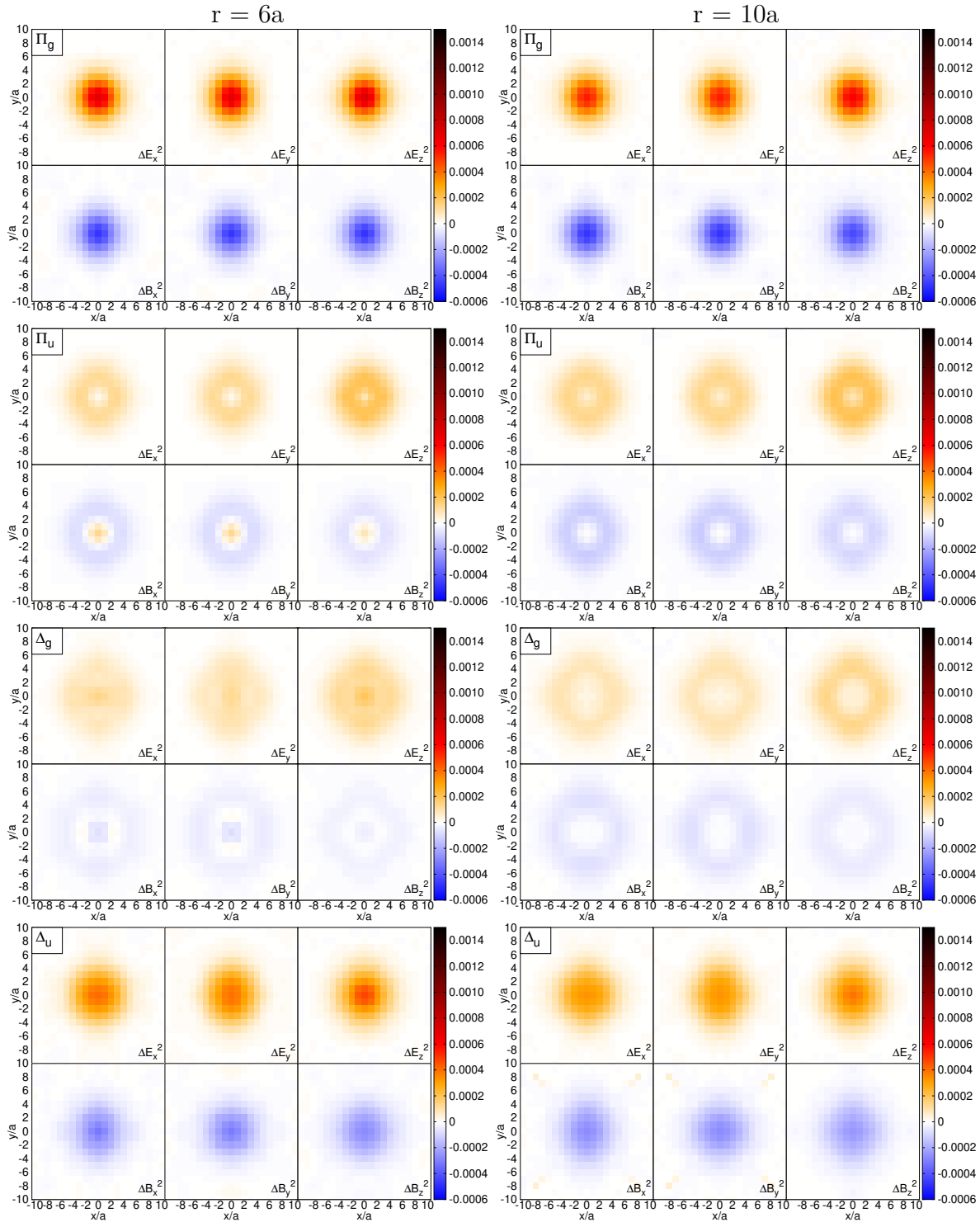

Figure A.2.: $\Delta F^2_{j,\Lambda_\eta^{(\epsilon)}}(r, \mathbf{x})$ for $\Lambda_\eta^\epsilon = \Pi_g, \Pi_u, \Delta_g, \Delta_u$ on the mediator plane for gauge group SU(3).
Left: $Q\bar{Q}$ - separation $r = 6a$.
Right: $Q\bar{Q}$ - separation $r = 10a$.

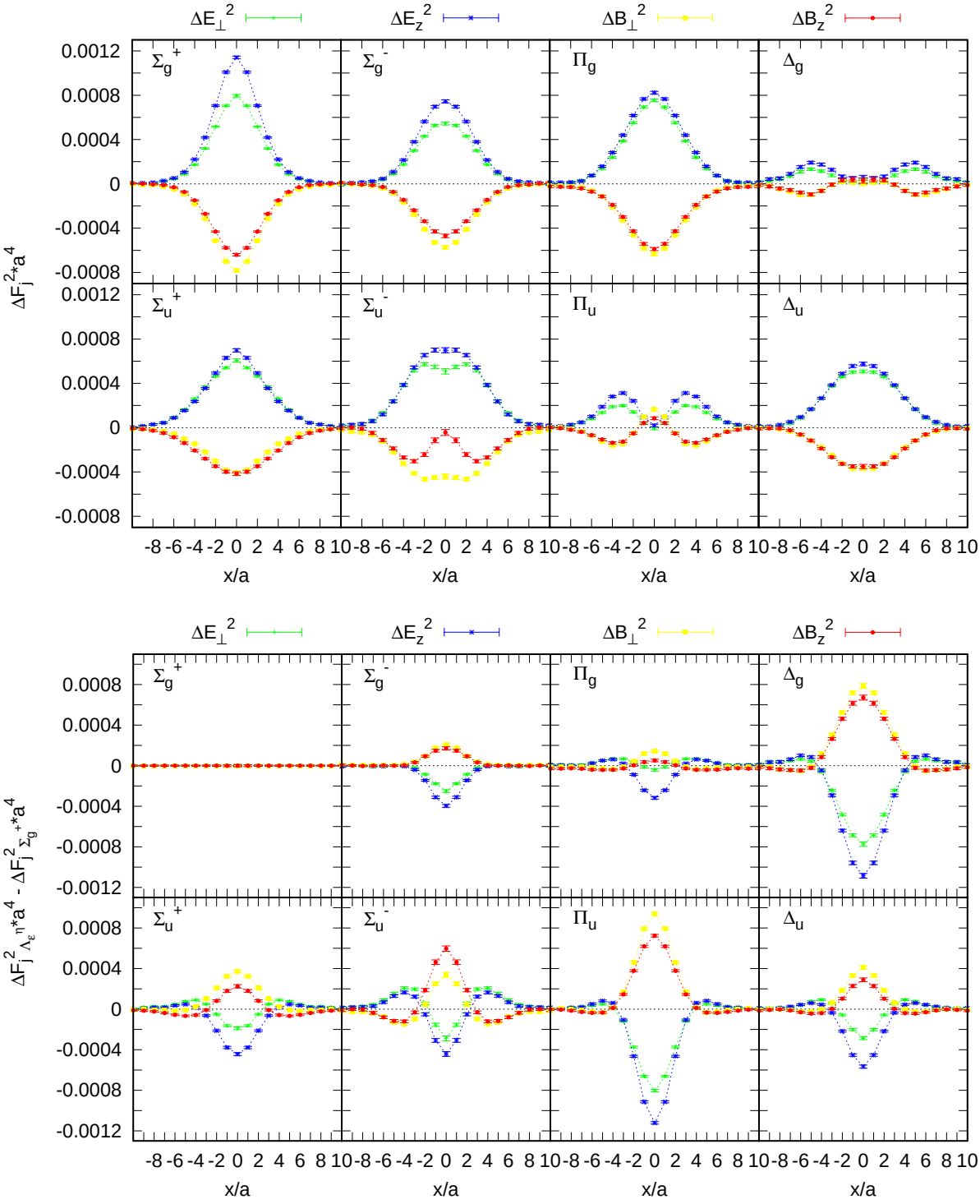

Figure A.3.: Flux densities on a mediator axis (x-axis) for $\Lambda_\eta^\epsilon = \Sigma_+^g, \Sigma_g^-, \Sigma_u^+, \Sigma_u^- \Pi_g, \Pi_u, \Delta_g, \Delta_u$, gauge group SU(3) and $Q\bar{Q}$ - separation $r = 10a$.
Top: $\Delta F^2_{j,\Lambda_\eta^{(\epsilon)}}(r, \mathbf{x})$ where $j \in \{\perp, z\}$
Bottom: $\Delta F^2_{j,\Lambda_\eta^{(\epsilon)}}(r, \mathbf{x}) - \Delta F^2_{j,\Sigma_g^+}(r, \mathbf{x})$ where $j \in \{\perp, z\}$

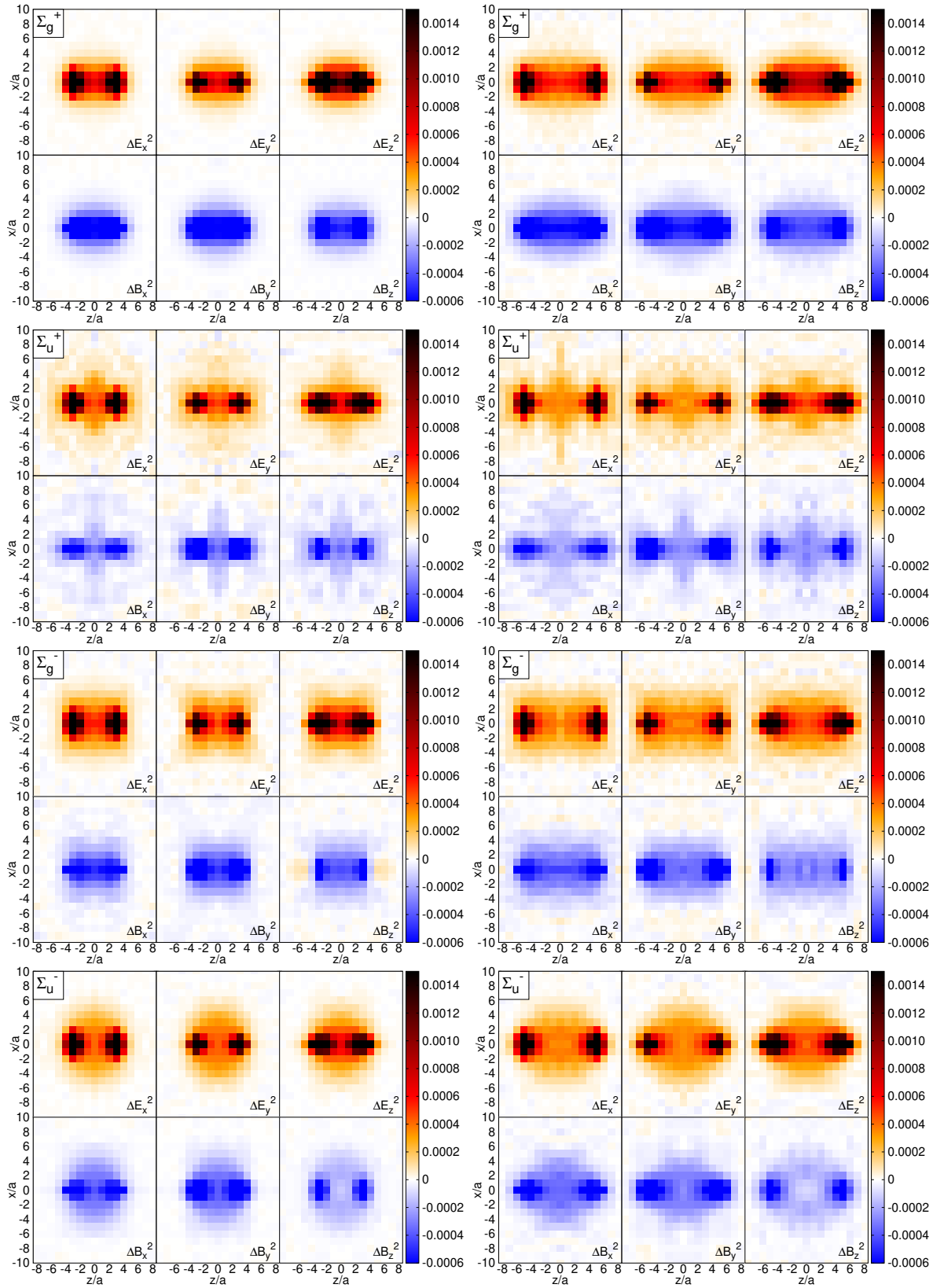

Figure A.4.: $\Delta F^2_{j,\Lambda^{(\epsilon)}_\eta}(r,\mathbf{x})$ for $\Lambda^\epsilon_\eta = \Sigma^g_+, \Sigma^-_g, \Sigma^+_u, \Sigma^-_u$ on the separation plane for gauge group SU(3).
Left: $Q\bar{Q}$ - separation $R = 6a$.
Right: $Q\bar{Q}$ - separation $R = 10a$.

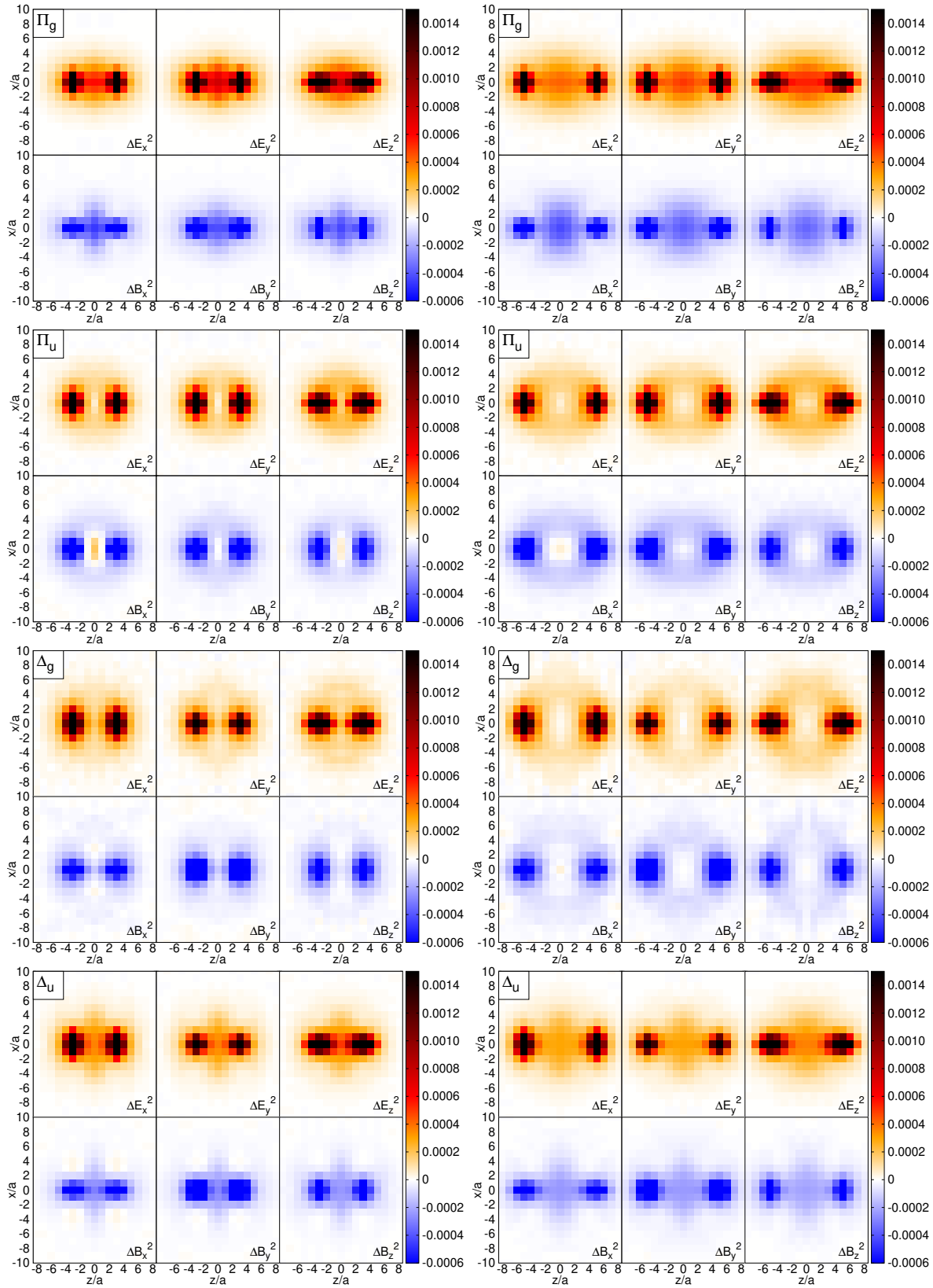

Figure A.5.: $\Delta F^2_{j,\Lambda^{(\epsilon)}_\eta}(r,\mathbf{x})$ for $\Lambda^\epsilon_\eta = \Pi_g, \Pi_u, \Delta_g, \Delta_u$ on the separation plane for gauge group SU(3).
Left: $Q\bar{Q}$ - separation $r = 6a$.
Right: $Q\bar{Q}$ - separation $r = 10a$.

Acknowledgements

First and foremost I want to thank Prof. Marc Wagner for the excellent supervision. He provided a lot of support not only on the matter but also in terms of promotion as a young scientist. In particular I am grateful for the opportunity to attend the "Excited QCD 2018" and "XIIIth Quark Confinement and the Hadron spectrum" conferences.
Next, I want to thank Christian Reisinger, who not only gave the basis for this work by delivering optimized operators for hybrid static potentials but also crosschecked our results and provided competent advice.
Finally, I also want to thank Francesca Cuteri for several useful discussions about flux tubes and Pedro Bicudo for interesting discussions about hybrid flux tubes.

Bibliography

[1] S. L. Olsen, T. Skwarnicki and D. Zieminska, "Nonstandard heavy mesons and baryons: experimental evidence," Rev. Mod. Phys. **9**0, 015003 (2018) [arXiv:1708.04012 [hep-ph]].

[2] L. A. Griffiths, C. Michael and P. E. L. Rakow, "Mesons with excited glue," Phys. Lett. **1**29B, 351 (1983).

[3] N. A. Campbell, L. A. Griffiths, C. Michael and P. E. L. Rakow, "Mesons with excited glue from SU(3) lattice gauge theory," Phys. Lett. **1**42B, 291 (1984).

[4] N. A. Campbell, A. Huntley and C. Michael, "Heavy quark potentials and hybrid mesons from SU(3) lattice gauge theory," Nucl. Phys. B **3**06, 51 (1988).

[5] C. Michael and S. J. Perantonis, "Potentials and glueballs at large beta in SU(2) pure gauge theory," J. Phys. G **1**8, 1725 (1992).

[6] S. Perantonis and C. Michael, "Static potentials and hybrid mesons from pure SU(3) lattice gauge theory," Nucl. Phys. B **3**47, 854 (1990).

[7] K. J. Juge, J. Kuti and C. J. Morningstar, "Gluon excitations of the static quark potential and the hybrid quarkonium spectrum," Nucl. Phys. Proc. Suppl. **6**3, 326 (1998) [hep-lat/9709131].

[8] M. J. Peardon, "Coarse lattice results for glueballs and hybrids," Nucl. Phys. Proc. Suppl. **6**3, 22 (1998) [hep-lat/9710029].

[9] K. J. Juge, J. Kuti and C. J. Morningstar, "A study of hybrid quarkonium using lattice QCD," AIP Conf. Proc. **4**32, 136 (1998) [hep-ph/9711451].

[10] C. Morningstar, K. J. Juge and J. Kuti, "Gluon excitations of the static quark potential," hep-lat/9809015.

[11] C. Michael, "Hadronic spectroscopy from the lattice: glueballs and hybrid mesons," Nucl. Phys. A **6**55, 12 (1999) [hep-ph/9810415].

[12] K. J. Juge, J. Kuti and C. J. Morningstar, "Ab initio study of hybrid $\bar{b}gb$ mesons," Phys. Rev. Lett. **8**2, 4400 (1999) [hep-ph/9902336].

[13] K. J. Juge, J. Kuti and C. J. Morningstar, "The heavy hybrid spectrum from NRQCD and the Born-Oppenheimer approximation," Nucl. Phys. Proc. Suppl. **8**3, 304 (2000) [hep-lat/9909165].

[14] C. Michael, "Quarkonia and hybrids from the lattice," PoS HF **8**, 001 (1999) [hep-ph/9911219].

[15] G. S. Bali *et* al. [SESAM and TχL Collaborations], "Static potentials and glueball masses from QCD simulations with Wilson sea quarks," Phys. Rev. D **6**2, 054503 (2000) [hep-lat/0003012].

[16] C. Morningstar, "Gluonic excitations in lattice QCD: a brief survey," AIP Conf. Proc. **6**19, 231 (2002) [nucl-th/0110074].

[17] K. J. Juge, J. Kuti and C. Morningstar, "Fine structure of the QCD string spectrum," Phys. Rev. Lett. **9**0, 161601 (2003) [hep-lat/0207004].

[18] C. Michael, "Exotics," Int. Rev. Nucl. Phys. **9**, 103 (2004) [hep-lat/0302001].

[19] K. J. Juge, J. Kuti and C. Morningstar, "The Heavy quark hybrid meson spectrum in lattice QCD," AIP Conf. Proc. **6**88, 193 (2004) [nucl-th/0307116].

[20] C. Michael, "Hybrid mesons from the lattice," hep-ph/0308293.

[21] G. S. Bali and A. Pineda, "QCD phenomenology of static sources and gluonic excitations at short distances," Phys. Rev. D **6**9, 094001 (2004) [hep-ph/0310130].

[22] K. J. Juge, J. Kuti and C. Morningstar, "Excitations of the static quark anti-quark system in several gauge theories," hep-lat/0312019.

[23] P. Wolf and M. Wagner, "Lattice study of hybrid static potentials," J. Phys. Conf. Ser. **5**99, 012005 (2015) [arXiv:1410.7578 [hep-lat]].

[24] C. Reisinger, S. Capitani, O. Philipsen and M. Wagner, "Computation of hybrid static potentials in SU(3) lattice gauge theory," EPJ Web Conf. **1**75, 05012 (2018) [arXiv:1708.05562 [hep-lat]].

[25] C. Reisinger, S. Capitani, L. Müller, O. Philipsen and M. Wagner, "Computation of hybrid static potentials from optimized trial states in SU(3) lattice gauge theory," arXiv:1810.13284 [hep-lat].

[26] S. Capitani, O. Philipsen, C. Reisinger, C. Riehl and M. Wagner, "Precision computation of hybrid static potentials in SU(3) lattice gauge theory," Phys. Rev. D **9**9, 034502 (2019) [arXiv:1811.11046 [hep-lat]].

[27] M. Fukugita and T. Niuya, "Distribution of chromoelectric flux in SU(2) lattice gauge theory," Phys. Lett. **1**32B, 374 (1983).

[28] J. W. Flower and S. W. Otto, "The field distribution in SU(3) lattice gauge theory," Phys. Lett. **1**60B, 128 (1985).

[29] J. Wosiek and R. W. Haymaker, "On the space structure of confining strings," Phys. Rev. D **3**6, 3297 (1987).

[30] A. Di Giacomo, M. Maggiore and S. Olejnik, "Evidence for flux tubes from cooled QCD configurations," Phys. Lett. B **2**36, 199 (1990).

[31] A. Di Giacomo, M. Maggiore and S. Olejnik, "Confinement and chromoelectric flux tubes in lattice QCD," Nucl. Phys. B **3**47, 441 (1990).

[32] P. Cea and L. Cosmai, "Lattice investigation of dual superconductor mechanism of confinement," Nucl. Phys. Proc. Suppl. **3**0, 572 (1993).

[33] G. S. Bali, K. Schilling and C. Schlichter, "Observing long color flux tubes in SU(2) lattice gauge theory," Phys. Rev. D **5**1, 5165 (1995) [hep-lat/9409005].

[34] P. Skala, M. Faber and M. Zach, "Magnetic monopoles and the dual London equation in SU(3) lattice gauge theory," Nucl. Phys. B **4**94, 293 (1997) [hep-lat/9603009].

[35] G. S. Bali, C. Schlichter and K. Schilling, "Probing the QCD vacuum with static sources in maximal Abelian projection," Prog. Theor. Phys. Suppl. **1**31, 645 (1998) [hep-lat/9802005].

[36] N. Cardoso, M. Cardoso and P. Bicudo, "Inside the SU(3) quark-antiquark QCD flux tube: screening versus quantum widening," Phys. Rev. D **8**8, 054504 (2013) [arXiv:1302.3633 [hep-lat]].

[37] P. Cea, L. Cosmai, F. Cuteri and A. Papa, "Flux tubes in the SU(3) vacuum: London penetration depth and coherence length," Phys. Rev. D **8**9, 094505 (2014) [arXiv:1404.1172 [hep-lat]].

[38] P. Cea, L. Cosmai, F. Cuteri and A. Papa, "Flux tubes at finite temperature," JHEP **1**606, 033 (2016) [arXiv:1511.01783 [hep-lat]].

[39] P. Cea, L. Cosmai, F. Cuteri and A. Papa, "Flux tubes in the QCD vacuum," Phys. Rev. D **9**5, 114511 (2017) [arXiv:1702.06437 [hep-lat]].

[40] P. Cea, L. Cosmai, F. Cuteri and A. Papa, "QCD flux tubes across the deconfinement phase transition," EPJ Web Conf. **1**75, 12006 (2018) [arXiv:1710.01963 [hep-lat]].

[41] M. Baker, P. Cea, V. Chelnokov, L. Cosmai, F. Cuteri and A. Papa, "Isolating the confining color field in the SU(3) flux tube," Eur. Phys. J. C **7**9, 478 (2019) [arXiv:1810.07133 [hep-lat]].

[42] M. Baker, P. Cea, V. Chelnokov, L. Cosmai, F. Cuteri and A. Papa, "Spatial structure of the color field in the SU(3) flux tube," PoS LATTICE **2**018, 253 (2018) [arXiv:1811.00081 [hep-lat]].

[43] P. Bicudo, M. Cardoso and N. Cardoso, "Colour fields of the quark-antiquark excited flux tube," EPJ Web Conf. **1**75, 14009 (2018) [arXiv:1803.04569 [hep-lat]].

[44] L. Müller and M. Wagner, "Structure of hybrid static potential flux tubes in SU(2) lattice Yang-Mills theory," Acta Phys. Polon. Supp. **1**1, 551 (2018) [arXiv:1803.11124 [hep-lat]].

[45] P. Bicudo, N. Cardoso and M. Cardoso, "Color field densities of the quark-antiquark excited flux tubes in SU(3) lattice QCD," Phys. Rev. D **9**8, 114507 (2018) [arXiv:1808.08815 [hep-lat]].

[46] L. Müller, O. Philipsen, C. Reisinger and M. Wagner, "Structure of hybrid static potential flux tubes in lattice Yang-Mills theory," PoS Confinement **1**3, 053 (2018) [arXiv:1811.00452 [hep-lat]].

[47] Heinz J. Rothe, *Lattice gauge theories: an introduction*, New Jersey [u.a.] : World Scientific Publ., 3rd edition, 2006

[48] L. Müller, "Investigation of the structure of hybrid static potential flux tubes", Bachelor of Science thesis at Goethe-Universität Frankfurt am Main (2018), [https://th.physik.uni-frankfurt.de/∼mwagner/theses/BA_Mueller.pdf].

[49] C. Reisinger, "Hybrid static potentials in SU(3) gauge theory on the lattice", Master of Science thesis at Goethe-Universität Frankfurt am Main (2017), [https://th.physik.uni-frankfurt.de/∼mwagner/theses/MA_Reisinger.pdf].

[50] R. G. Edwards *et* al. [SciDAC and LHPC and UKQCD Collaborations], Nucl. Phys. Proc. Suppl. **1**40, 832 (2005) doi:10.1016/j.nuclphysbps.2004.11.254 [hep-lat/0409003].

[51] K. Jansen *et* al. [ETM Collaboration], JHEP **0**812, 058 (2008) doi:10.1088/1126-6708/2008/12/058 [arXiv:0810.1843 [hep-lat]].

[52] A. Hasenfratz and F. Knechtli, "flavour symmetry and the static potential with hypercubic blocking," Phys. Rev. D **6**4, 034504 (2001) [arXiv:hep-lat/0103029].

[53] M. Della Morte *et* al., "Lattice HQET with exponentially improved statistical precision," Phys. Lett. **B**581, 93, (2004) [arXiv:hep-lat/0307021].

[54] M. Della Morte, A. Shindler and R. Sommer, "On lattice actions for static quarks," JHEP **0**508, 051 (2005) [arXiv:hep-lat/0506008].

[55] http://www.physics.utah.edu/%7Edetar/phycs6730/handouts/jackknife/jackknife/, date: 08.07.2019

[56] M. Berwein, N. Brambilla, J. Tarrus Castella and A. Vairo, "Quarkonium Hybrids with Nonrelativistic Effective Field Theories," Phys. Rev. D **9**2, 114019 (2015) [arXiv:1510.04299 [hep-ph]].

[57] N. Brambilla, A. Pineda, J. Soto and A. Vairo, "Potential NRQCD: an effective theory for heavy quarkonium," Nucl. Phys. B **5**66, 275 (2000) [hep-ph/9907240].